JGR Space Physics

RESEARCH ARTICLE
10.1029/2024JA032656

Rapid Geomagnetic Variations During High-Speed Stream, Sheath and Magnetic Cloud-Driven Geomagnetic Storms From 1996 to 2023

M. N. Pedersen[1], L. Juusola[2], H. Vanhamäki[1], A. T. Aikio[1], and A. Viljanen[2]

[1]Space Physics and Astronomy Research Unit, University of Oulu, Oulu, Finland, [2]Finnish Meteorological Institute, Helsinki, Finland

Key Points:

- This paper presents a catalog of geomagnetic storms, their phases and interplanetary drivers from 1996 to 2023
- During the storm sudden commencement three hotspots of spikes in $|d\boldsymbol{H}_{ext}/dt|$ exist, at 04, 09 and 15 magnetic local time
- Sheath storms have $|d\boldsymbol{H}_{ext}/dt|$ spikes occurring during the entire main phase, while for MC and HSS/SIR peak toward the end of the main phase

Supporting Information:

Supporting Information may be found in the online version of this article.

Correspondence to:

M. N. Pedersen,
marcus.pedersen@oulu.fi

Citation:

Pedersen, M. N., Juusola, L., Vanhamäki, H., Aikio, A. T., & Viljanen, A. (2024). Rapid geomagnetic variations during high-speed stream, sheath and magnetic cloud-driven geomagnetic storms from 1996 to 2023. *Journal of Geophysical Research: Space Physics*, *129*, e2024JA032656. https://doi.org/10.1029/2024JA032656

Received 15 MAR 2024
Accepted 25 SEP 2024

Abstract The most detrimental geomagnetically induced currents (GICs) documented to date have all taken place during geomagnetic storms. Yet, the probability of GICs throughout geomagnetic storms driven by different solar wind transients, such as high-speed streams/stream interaction regions (HSS/SIR) or interplanetary coronal mass ejection (ICME) sheaths and magnetic clouds (MC), is poorly understood. We present an algorithm to detect geomagnetic storms and storm phases, resulting in a catalog of 755 geomagnetic storms from January 1996 to June 2023 with the solar wind drivers. Using these storms and the IMAGE magnetometer network, we study the temporal and spatial evolution of spikes in the time derivative of the horizontal component of the external magnetic field, $|d\boldsymbol{H}_{ext}/dt|$, greater than 0.5 nT/s during geomagnetic storms driven by HSS/SIR, sheaths and MCs. Spikes occur more often toward the end of the storm main phase for HSS/SIR and MC-driven storms, while sheaths have spikes throughout the entire main phase. During the main phase most spikes occur in the morning sector around 05 magnetic local time (MLT) and the extent in MLT is narrowest for MCs and widest for sheaths. However, spikes in the pre-midnight sector during the main and recovery phases are most prominent for HSS/SIR-driven storms. During the storm sudden commencement (SSC), three MLT hotspots exist, the post-midnight at 04 MLT, pre-noon at 09 MLT and afternoon at 15 MLT. The pre-noon hotspot has the highest probability of spikes and the widest extent in magnetic latitude.

Plain Language Summary Geomagnetic storms can have damaging implications on technological infrastructures such as power grids, pipelines or railway systems. Those implications arise due to geomagnetically induced currents (GICs) caused by rapid changes in the Earth's magnetic field. In this paper, we present a way to automatically detect geomagnetic storms as well as the key periods of the storm's activity. The primary solar wind structures that cause geomagnetic storms are high-speed streams and their stream interaction regions (HSS/SIR), sheaths ahead of interplanetary coronal mass ejections and magnetic clouds (MC). Using the detected geomagnetic storms we study spikes in the magnetic field changes in Fennoscandia to map the GIC activity throughout the geomagnetic storms caused by HSS/SIR, sheaths and MCs. We report on several similarities and differences in the evolution and extent of spikes during geomagnetic storms for the different solar wind structures. One such difference is for example, in the likelihood of spikes throughout the storm. For those storms caused by HSS/SIR and MCs spikes are more likely close to the time of maximum geomagnetic storm disturbance, while for storms caused by sheaths spikes are likely at any time from the beginning of the storm to the maximum storm disturbance.

1. Introduction

A geomagnetic storm is a large-scale disturbance in the Earth's magnetosphere caused by energetic solar wind transients. The intensity of geomagnetic storms is monitored using the (1 min resolution) SYM-H index (or 1 hr resolution Dst index) computed from mid-latitude ground magnetometers that measure the Earth's ring current (Burton et al., 1975; Iyemori, 1990; Sugiura, 1963; Wanliss & Showalter, 2006). A geomagnetic storm commonly has three phases: a main phase that starts when the ring current begins to grow and ends when it reaches maximum intensity, a recovery phase that lasts from the end of the main phase until the ring current is back to pre-storm conditions, and occasionally an initial phase that precedes the main phase when a sudden change in solar wind dynamic pressure compresses the magnetopause before the enhancement of the ring current (see e.g. Burton et al., 1975). Most of the weak-to-moderate geomagnetic storms are caused by solar wind high-speed streams and their stream interaction region (HSS/SIR), while the most intense geomagnetic storms are caused by sheaths in

front of interplanetary coronal mass ejections (ICMEs) or magnetic clouds (MCs) embedded in the ICME (Bothmer & Schwenn, 1995; Kamide et al., 1998).

Geomagnetic storms can cause widespread damage to technological infrastructures such as power grids, pipelines or railway systems through geomagnetically induced currents (GICs). GICs occur as a result of rapid changes in the ground magnetic field, and therefore the amplitude of the time derivatives of the horizontal magnetic field at ground level, $|d\boldsymbol{H}/dt|$, are often used as a proxy of GIC activity (e.g., Bolduc et al., 1998; Viljanen et al., 2001). These ground magnetic field fluctuations are caused by rapidly varying external currents in the ionosphere and magnetosphere. However, a large fraction of the contribution to the measured $|d\boldsymbol{H}/dt|$ comes from telluric currents induced in the Earth's ground that are highly dependent on the local conductivity structure (e.g., Juusola et al., 2023; Tanskanen et al., 2001). Pulkkinen et al. (2017) presented an overview of the current status of GICs and the challenges ahead. They stated that in terms of model forecasting of GIC, distinguishing the impact of different interplanetary transient features, such as shocks, sheaths, MC and ejecta of ICMEs have on producing GIC may help improve forecasting.

Hajra (2022) studied 605 intense GICs in southern Finland, of which only one occurred during geomagnetically quiet times. For the storm time GICs, 72% occurred during the storm main phase and 28% during the storm recovery phase. Of these, 50.8% were caused by sheaths, 44% were caused by MC and 0.2%/3.1% by HSS/SIR. Kataoka and Pulkkinen (2008) found that the amplitude of GICs is relatively small during HSS/SIR storms compared to ICME storms, but that GICs related to Kelvin-Helmholtz instabilities and pulsations in the prenoon sector are more frequent and longer lasting during HSS/SIR storms. Huttunen et al. (2008) found that the largest GICs are most likely to take place during the passage of the ICME sheaths and may even occur when no activity is seen in terms of the Dst index. On the contrary, GICs by the ejecta needed significant geomagnetic activity in terms of the Dst index. Although ICMEs cause the largest GICs, it has been reported that GICs occur preferentially in the declining phase of the solar cycle, which is the time when HSS/SIR-driven storms are most frequent (Juusola et al., 2015; Tsurutani et al., 2006).

The likelihood of GICs and large $|d\boldsymbol{H}/dt|$ depend both on the magnetic latitude (MLAT) and magnetic local time (MLT). It has become clear that there are at least two MLT hotspots, one in the pre-midnight sector associated with substorm onsets and one in the morning sector associated with the passage of omega bands (e.g., Juusola et al., 2015; Viljanen et al., 2001). Recently, a third and smaller hotspot has been reported in the pre-noon sector and is thought to be caused by Kelvin-Helmholtz-instabilities at the magnetopause propagating through field-line oscillations (e.g., Milan, Imber, et al., 2023).

A few studies have separated the internal (telluric) and external (ionospheric and magnetospheric) parts of the magnetic field (e.g., Juusola et al., 2020, 2023; Kellinsalmi et al., 2022; Pulkkinen et al., 2003). We adhere to that notion and investigate only the external part of the horizontal magnetic field change, $|d\boldsymbol{H}_{ext}/dt|$. This makes the results independent of the local ground conductivity structure since $|d\boldsymbol{H}_{ext}/dt|$ is solely caused by external currents. In this study, we try to address some of the challenges laid out by Pulkkinen et al. (2017) and investigate both the temporal and spatial development of large $|d\boldsymbol{H}_{ext}/dt|$ during geomagnetic storms driven by HSS/SIR, sheaths and MCs from 1996 to 2023.

The paper is organized as follows: in Section 2.1 we present an algorithm to detect geomagnetic storms and storm phases using the SYM-H index. In Section 2.2 the storms detected are cross-referenced with catalogs of solar wind transients passing Earth to identify the storm drivers. Section 2.3 describes the analysis method used to study the rapid geomagnetic variations. Sections 3.1 and 3.2 show the results of the temporal and spatial evolution of spikes during the geomagnetic storms detected, respectively. Section 4 contains a more in-depth discussion of the results and a comparison to existing literature. Section 5 presents the conclusions.

2. Data and Methods

2.1. Automated Identification of Geomagnetic Storms and Their Phases

We developed an algorithm to detect geomagnetic storms and the storm phases using the SYM-H index (Iyemori, 1990). The interplanetary drivers were identified by cross-referencing the storms with the HSS/SIR catalog by Grandin et al. (2019) and ICME catalog by Cane and Richardson (2003) as will be explained in Section 2.2. To detect geomagnetic storms and the storm phases the following algorithm was applied to the SYM-H index.

1. Find all continuous sequences in SYM-H with values less than −15 nT and with a minimum SYM-H value ≤ − 50 nT. The beginning and end times of this sequence occur when the ring current has slightly more energy than during quiet times and the minimum SYM-H requirement ensures that the geomagnetic storm is of at least moderate intensity (Loewe & Prölss, 1997).
2. To determine the main phase onset time, include 3 hr of SYM-H data prior to the beginning of the above sequence and set the main phase onset to the time the SYM-H crossed 0 nT, or to the time of largest (closest to zero) SYM-H if there is no zero crossing. This is intended to ensure that the beginning of the main phase is set to the time the ring current starts growing.
3. The end of the main phase is set to the time of the minimum SYM-H index. The storm recovery phase begins after the end of the storm main phase and lasts till the end of the sequence when the SYM-H index has recovered to more than −15 nT.
4. A search for a storm sudden commencement (SSC) before the main phase onset is done by looking for SYM-H increases of at least 10 nT in 3 min or less on the interval up to 24 hr before main phase onset (based on Joselyn & Tsurutani, 1990). In the cases where several such SYM-H increases are detected before the main phase onset, the first time it occurs is set as the time of SSC and a storm initial phase is set to commence at the SSC and end at storm main phase onset.

It is worth noting that while the end of the main phase is strictly defined as the minimum of the SYM-H index, the main phase onset is much more difficult to pinpoint. This is because the beginning of the decrease in the SYM-H index is not well defined and for most storms the index does not decrease monotonically throughout the main phase. Therefore, precise determination of the main phase onset time based on the first decrease in the SYM-H index is prone to some uncertainty and speculations. Several different ways to pinpoint the main phase onset have been used, from manual inspection (e.g., Hutchinson et al., 2011), machine learning (Balan et al., 2017), the time the Dst or SYM-H index crossed zero (e.g., Yokoyama & Kamide, 1997) or the time it crossed to −15 nT (e.g., Pedersen et al., 2021; Walach & Grocott, 2019). Our approach above is a combination of the latter two methods and is fully automated. Figure 1 top panel shows the SYM-H index and storm phases for one of the storms detected using the above algorithm with shading highlighting the initial (green), main (blue) and recovery (red) phases.

A small number of storms detected had a main or recovery phase of less than 25 min. From visual inspection of the solar wind and interplanetary magnetic field (IMF) data for each storm, these short main phases and recovery phases were solely caused by high-density plasma parcels hitting upon the magnetopause, enhancing the magnetopause current that caused a positive and negative jump in the SYM-H index with just minutes in between. Therefore, storms with a main phase or recovery phase duration of <25 min have been merged with adjacent storms or removed. The SSCs detected using the above criteria are in good agreement with the SSCs reported by Ebro Observatory, which is entrusted by the International Association of Geomagnetism and Aeronomy (IAGA) to administer and report rapid magnetic variations and among them sudden commencements (Curto et al., 2007). In total, 70% of the SSCs detected are also reported by Ebro Observatory within ±3 min.

2.1.1. Compound Geomagnetic Storms

Sometimes the SYM-H index does not fully recover to −15 nT following a geomagnetic storm before the onset of a second clear depression. To detect significant compound storms of this kind, where one storm immediately follows the other, we use the concept of prominence of local extrema. The prominence of a local minimum in the SYM-H index is defined as the lowest increase necessary before reaching another lower minimum. This is illustrated in the top panel of Figure 2, where the black circle shows a local SYM-H minimum of −391 nT and the gray circle shows the local SYM-H maximum of −76 nT. The prominence of the local minimum is 315 nT and is shown by the vertical line. The following steps and criteria are used in the analysis of compound storms.

I. To distinguish only significant compound storms, local minima in the SYM-H must have a prominence that is at least 1/3 of the absolute value of the global minimum in the SYM-H sequence or 50 nT, whichever is largest.
II. The end of the previous recovery phase and the next main phase onset are set to the time of the maximum SYM-H value between the minima found in Step I. The end of the last recovery phase of a compound storm is the end time of the original sequence.

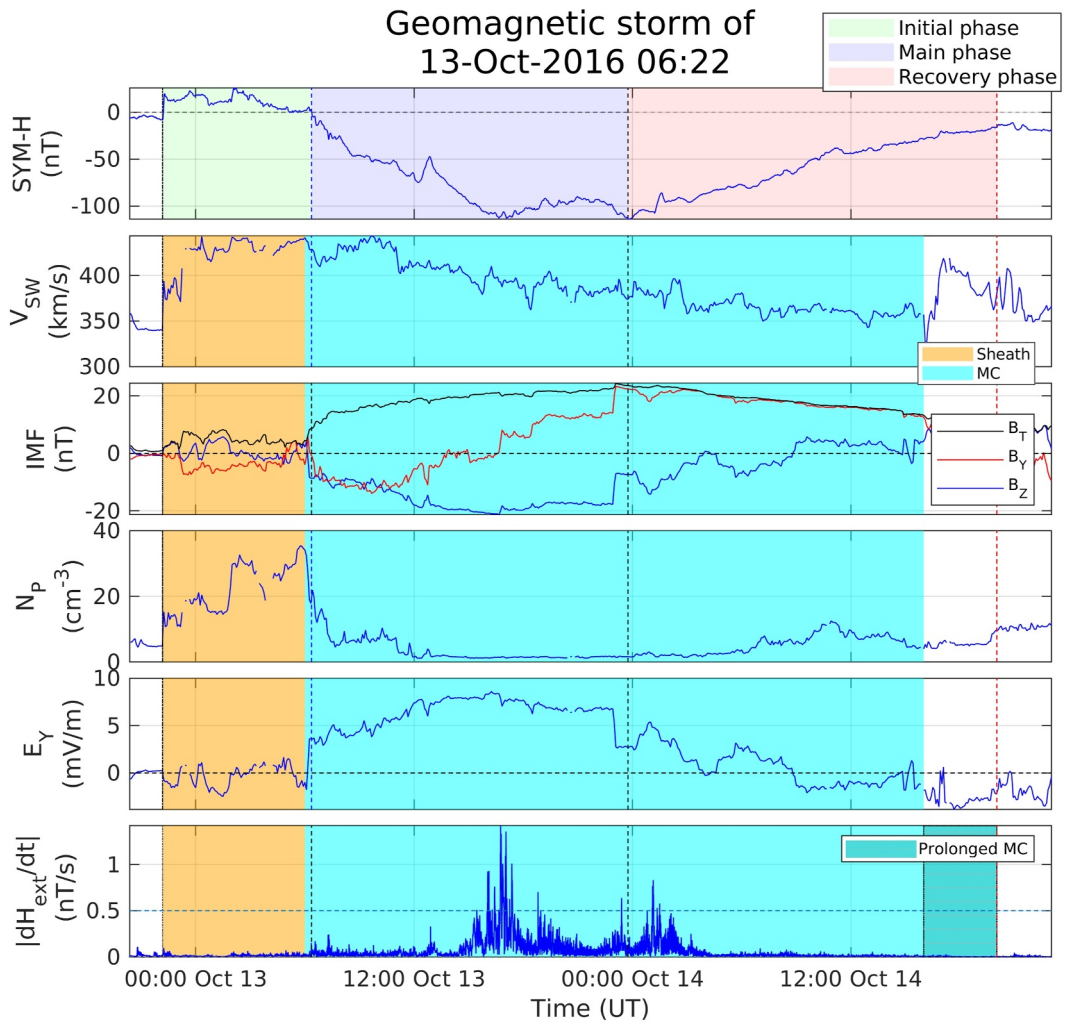

Figure 1. The top panel shows the SYM-H index for the geomagnetic storm on the thirteenth of October 2016. In the top panel, the shaded region shows the initial phase (green), main phase (blue) and recovery phase (red) of the storm. The second to fifth panels show the 5 min resolution solar wind parameters and interplanetary magnetic field in geocentric solar magnetospheric (GSM) coordinates from OMNI during the time of the storm, and the shading indicates the active solar wind driver at that time. The bottom panel shows $|d\boldsymbol{H}_{ext}/dt|$ at Nurmijärvi station (56.9° MLAT) with the 0.5 nT/s limit by a dashed line. The dashed vertical lines in all panels are the boundaries between the storm phases. In the bottom panel, the MC-driver has been extended until the end of the storm recovery phase as explained in Section 2.3. Time is in Universal Time (UT).

III. Each compound storm must have a main phase duration ≥2 hr and recovery phase duration ≥10 hrs. This criterion follows the procedure of Balan et al. (2017) and satisfies typical recovery phase durations (e.g., Yermolaev et al., 2014).

The restriction on main phase duration in Step III does not apply to the first storm in the compound event, and the recovery phase restriction does not apply to the last storm of the event - to make the beginning and ends leading to quiet time conditions have the same restrictions as other storms. In these cases where the minimum main or recovery phase durations are not met, the two candidate storms are considered as a single storm. The reason for having a longer restriction time for the main and recovery phases that separate compound storms than those leading to quiet conditions was to ensure that compound storms are in fact separate storms.

Figure 2 shows the October 2003 Halloween storm which was separated into two storms following the algorithm above. The figure has added markers indicating some relevant values and times. The prominence of the less intense storm is larger than the threshold defined in Step I and the recovery phase and main phase durations of the compound storms are longer than the minimum durations required in Step III.

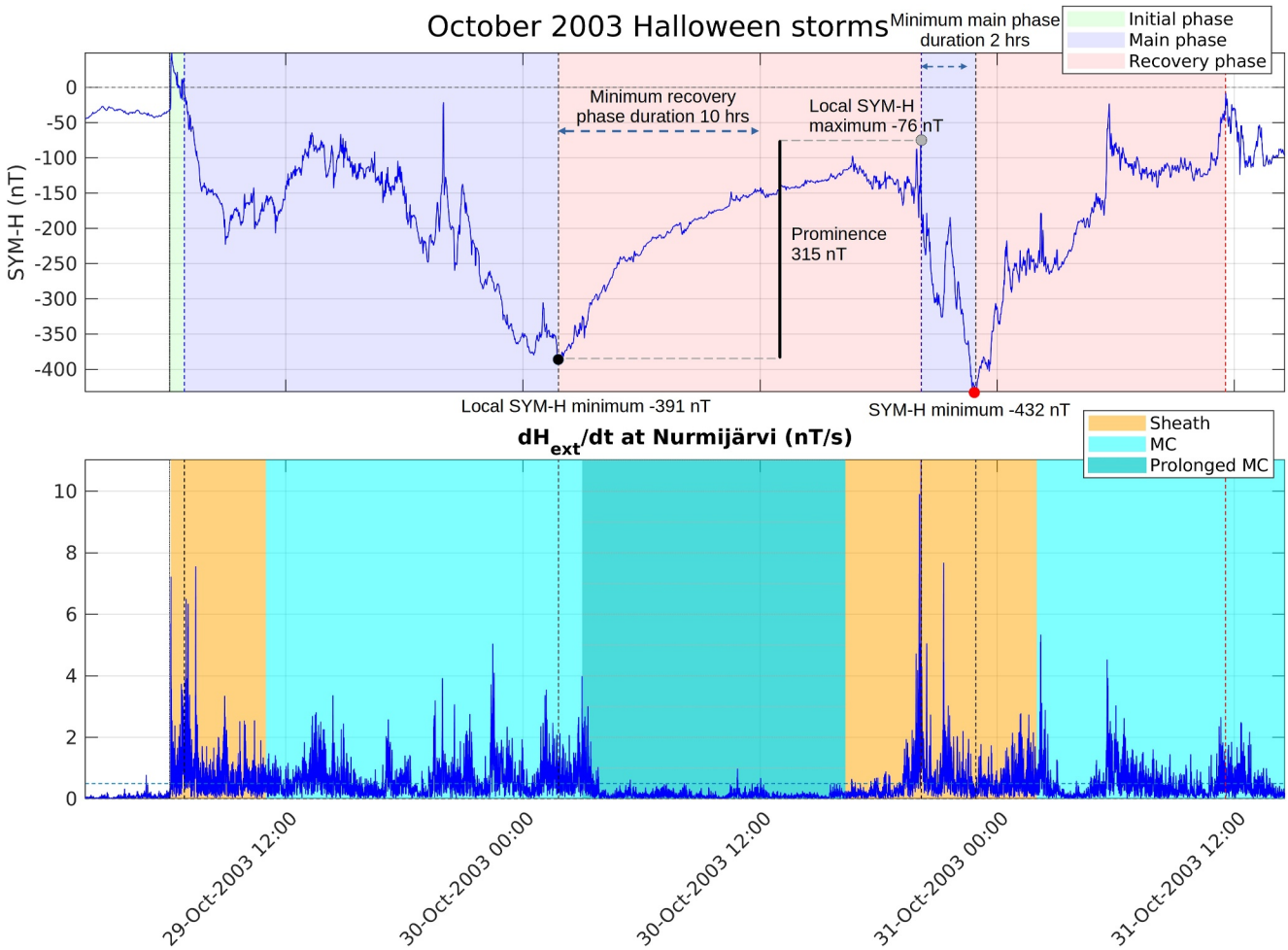

Figure 2. The top panel shows the SYM-H index for the October 2003 Halloween storms, which is an example of a compound event. The black and red circles show two minima in the SYM-H index with the black circle being a local minimum and red the global minimum. The black vertical line shows the prominence of the local minimum in the SYM-H index. The blue horizontal dashed lines show the minimum allowed recovery phase and main phase durations for compound storms used in step 3. All criteria were satisfied and so the originally detected storm was separated into two storms as shown. The bottom panel shows $|d\boldsymbol{H}_{ext}/dt|$ at Nurmijärvi station during this extreme event.

In total 755 storms were detected from January 1996 to June 2023, of which 17 emerged from compound storms. It should be noted that the detection of compound storms was done solely based on the SYM-H index and requires typical main and recovery phase durations. Many studies refer to geomagnetic storms driven by the interaction of several CMEs or HSSs/SIRs as complex storms, and complex storms often have multiple peaks in the SYM-H index and prolonged geomagnetic activity (e.g., Vennerstrom et al., 2016). Those storms will be discussed further in Section 2.2 where we identify the solar wind drivers.

The software to detect geomagnetic storms and storm phases described in this section can be accessed at https://doi.org/10.5281/zenodo.12699343 along with figures of the SYM-H index, solar wind/IMF parameters and the solar wind drivers for each of the 755 storms.

2.2. Identifying the Solar Wind Driver

To find the interplanetary drivers active during the storms, the storms detected were cross-referenced with the ICME catalog by Cane and Richardson (2003) which is regularly updated and can be accessed at https://doi.org/10.7910/DVN/C2MHTH, and an extended HSS/SIR catalog by Grandin et al. (2019). Because these catalogs do not extend further than 1996, solar wind drivers are only identified for storms between January 1996 and June 2023. The ICME catalog has an indicator of whether the ejecta is likely to be an MC. To get a candidate group of

Table 1
Median Values of Selected Parameters and Their Median Absolute Deviations During the Studied Storms, Categorized Based on the Interplanetary Driver

	HSS/SIR	Sheath	MC	Ejecta without MC
Number of storms (605)	297	101	168	39
Median main phase	7.6 ± 3.7 hr	5.7 ± 3.5 hr	8.9 ± 4.4 hr	7.6 ± 4.5 hr
Median recovery phase	25 ± 15 hr	18 ± 14 hr	27 ± 16 hr	27 ± 16 hr
Median minimum SYM-H	−62 ± 8 nT	−89 ± 26 nT	−90 ± 26 nT	−72 ± 13 nT
Minimum SYM-H in category	−137 nT	−432 nT	−490 nT	−228 nT
Number of SSC (218)	51	134	19	14
Median initial phase	3.0 ± 2.2 hr	5.0 ± 3.7 hr	1.7 ± 1.6 hr	1.8 ± 1.7 hr
Median ΔSYM-H (nT/3 min) at SSC	11 ± 1	14 ± 3	11 ± 1	11 ± 1
Max ΔSYM-H (nT/3 min) at SSC	26	63	19	44

Note. In the first five rows, the category is based on the driver that is active during most of the main phase. In the last four rows it is based on the driver causing the SSC.

MCs and sheaths, we found the ICME storms where the ejecta is MC flagged and then checked what parts of the storm occurred during the ejecta or the disturbed region ahead of the ejecta known as the sheath region. As Cane and Richardson (2003) use multiple detection methods to identify ICMEs, while the Grandin et al. (2019) HSS/SIR detection method is fully automated and tries to remove HSS/SIR influenced by ICMEs, in all cases where there are conflicts between the ICME and HSS/SIR catalogs the driver was set according to the ICME list. On exceptional occasions, Cane and Richardson (2003) ICME list reports a new disturbed region during the time of an already ongoing ejecta. From visual inspection of the solar wind and IMF during many of those cases, it is seen that they mostly resemble sheath signatures, and have therefore been classified as sheath periods in this study.

In our geomagnetic storm catalog, which can be found in the supplementary material, four different solar wind drivers are reported: HSS/SIR, sheaths, MCs and ejecta without MCs. The sheath category includes both sheaths with and without interplanetary shocks. Ejecta without MC signatures caused far fewer geomagnetic storms than any of the other drivers and were therefore not included in the remaining of this study. Figure 1 panels two through four show the 5 min OMNI solar wind velocity, IMF and solar wind density propagated to the Earth's bowshock nose during a geomagnetic storm driven by an ICME's sheath and MC (King & Papitashvili, 2005). The yellow shading shows the passage of the sheath region and the light blue shows the MC. Typical characteristics of sheaths, such as dense plasma and turbulent IMF can be seen, and for the MCs the smoothly rotating IMF structure is clearly visible.

To evaluate the list of geomagnetic storms, we compared our catalog with other lists of geomagnetic storms. Sandhu et al. (2021) published a list of geomagnetic storms and storm phases between 2012 and 2018 using the method by Walach and Grocott (2019). We detect all of their storms and have the same recovery phase start and end times. The main phase onset is always detected slightly earlier (on average 56 min, upto a maximum of 180 min) in our catalog because of criteria two in Section 2.1 which attempts to pinpoint the onset to a time when SYM-H is closer to the zero crossing. For the initial phase we apply a stricter requirement and must detect an SSC, which is not comparable to their initial phase start times. Furthermore, five of their storms were detected as compound storms following Section 2.1.1 and separated in our storm catalog, which included the complex storms on 18 February 2014 (which has been studied by e.g. Durgonics et al., 2017) and 7–9 September 2017 (Kumar & Kumar, 2020).

We also compared our catalog to Ahmed et al. (2024) who provided a list of 57 carefully selected ICME and HSS/SIR storms from 1995 to 2019. All of their storms were detected by our storm catalog, and the identified solar wind drivers for these storms are mostly in good agreement. Of the 55 storms after 1996 in their list, we identify the same solar wind drivers in 44 storms (80%). For the remaining 11 storms, we identify some part of the ICME differently (e.g., MC instead of ejecta without MC) and in one storm we do not identify the HSS/SIR reported in their list. It should be emphasized that for the interplanetary drivers we use the catalogs of Grandin et al. (2019)

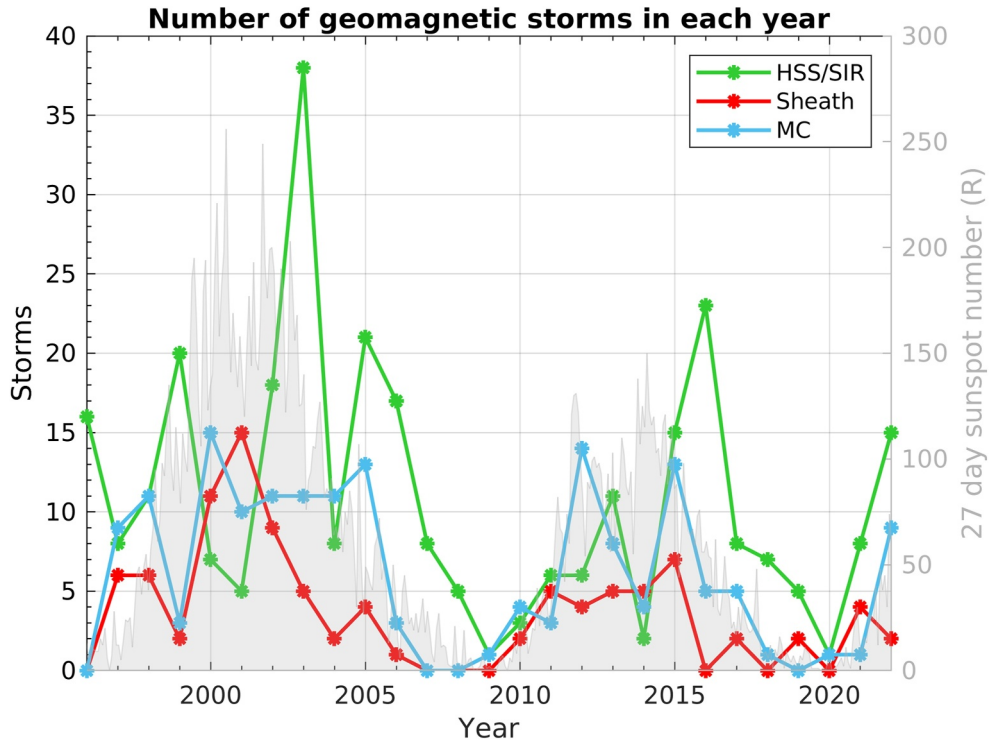

Figure 3. Number of storms and the primary interplanetary drivers (see legend) during the storm main phase from 1996 till the end of 2022. The gray shaded area shows the 27 day averaged sunspot number.

and Cane and Richardson (2003) as is. These are two widely used catalogs of HSSs/SIRs and ICMEs passing by Earth. However, the interested reader can use our storm catalog with any other list of interplanetary structures.

In our storm catalog, 47 storms (6.2%) are influenced by more than one ICME or HSSs/SIRs during the storm main phase, while there are 134 (17.8%) such storms when all storm phases are considered. This shows that many of the storms in our list might be considered complex storms, albeit they are reported as a single storm because their evolution in terms of the SYM-H index does not fulfill the requirements of a compound storm as described in Section 2.1.1. Nevertheless, the separation into compound events captured several well-known complex storms, for example, the two Halloween storms on the 29th and 30th of October 2003, seen in Figure 2, which have been studied extensively (e.g., Weaver, 2004) and the complex storm on 7–9 of September 2017 (e.g., Blagoveshchensky & Sergeeva, 2019; Kumar & Kumar, 2020).

Table 1 summarizes the main properties of the storms in our catalog. The storms are categorized by the primary solar wind driver that was responsible for the largest fraction of the storm's main phase. The top rows show the median values and median absolute deviations (MADs) of the phase durations and storm intensity. Most storms are caused by HSS/SIR and the fewest by ejecta without MC signatures. HSS/SIR storms are generally the weakest, while the most intense storms are caused by sheaths and MCs. The bottom rows of Table 1 categorize the solar wind driver causing the SSC. To account for slight uncertainty in the arrival times of new interplanetary structures, the driver causing the SSC was set as the interplanetary structure present for the majority of the time from the beginning of the SSC to 20 min after. Of the 218 SSCs, 134 (i.e., 62%) are caused by the arrival of sheath regions ahead of ICME ejecta. Figure 3 shows the yearly distribution of storms and the primary solar wind driver for each year from 1996 to the end of 2022 with the 27 day average sunspot number.

Figure 4 shows the primary interplanetary driver as a percentage of all storms divided into ranges of minimum SYM-H index (storm intensity). Only storms with identified solar wind drivers are included in Figure 4. HSS/SIR are responsible for 67% of storms within the lowest SYM-H index range of −50 to −74 nT, while ICME storms are responsible for the majority of storms with SYM-H index less than −100 nT and all storms with SYM-H index less than −137 nT (Table 1). The majority of the ICME-driven storms are caused by MCs, but the fraction of sheath-driven storms becomes larger for more intense storms and accounts for 41% for all storms with minimum

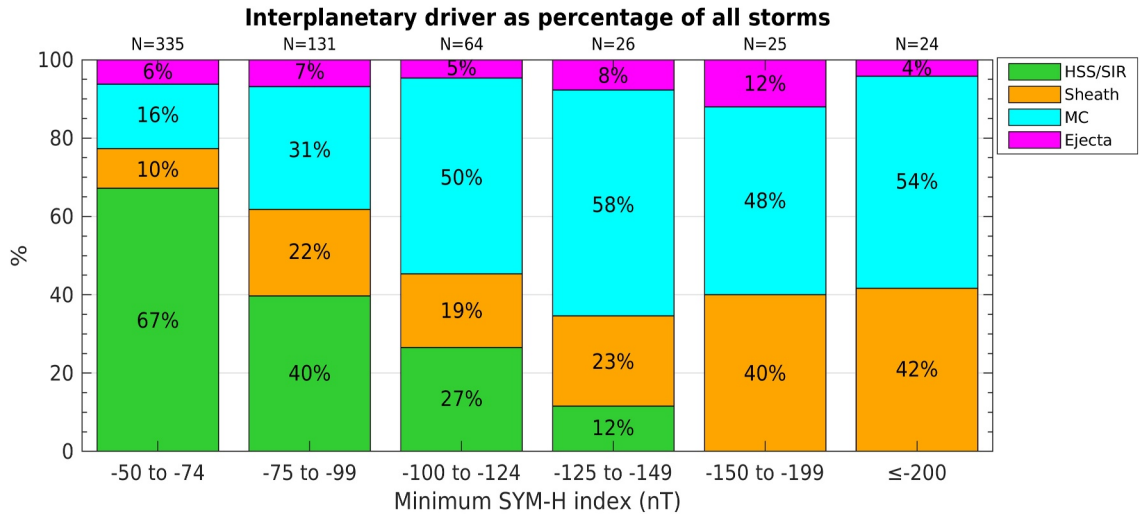

Figure 4. Percentage of geomagnetic storms categorized by primary interplanetary driver during the storm main phase, separated into six minimum SYM-H index ranges. The number N above each bar is the total number of storms within that range. The first four intervals are 25 nT wide, the fifth interval is 50 nT wide and the last interval is storms with minimum SYM-H index −200 nT or less.

SYM-H less than −150 nT. The number of storms in each bin decreases rapidly with a decreasing minimum SYM-H index resulting in a heavy-tailed distribution driven solely by ICME storms. In addition to the storms in Figure 4 there are 150 storms with unidentified solar wind drivers, whereof 123 are in the range of the first bin with minimum SYM-H index between −50 and −74 nT, 20 in the second bin and 7 in the third bin. All storms with SYM-H index less than −125 nT between 1996 and June 2023 have identified solar wind drivers.

In the supplementary material we provide a catalog of the geomagnetic storms, their phases and the solar wind drivers from January 1996 to June 2023. The supplementary material also includes an extended list of all geomagnetic storms and their phases detected by our algorithm from the beginning of the year 1981 to 2024. However, for the remainder of this article, we only study the storms between January 1996 and June 2023.

2.3. Analysis of Rapid Geomagnetic Variations From IMAGE Data

The 10 s ground magnetic field measurements from the International Monitor for Auroral Geomagnetic Effects (IMAGE) magnetometer network were used from 1996 to 2023. Figure 5 shows the IMAGE stations used in this study, with the Nurmijärvi station that was used in Figures 1 and 2 marked in blue. Only IMAGE stations with magnetic latitude (MLAT) above 54° and with data covering more than 5 years have been included in this study (see https://space.fmi.fi/image/ for a list of all IMAGE stations and their data availability). The requirement of at least 5 years of data coverage ensures that each station has a sufficient number of measurements to reliably determine probabilities and not be too heavily influenced by a short portion of a solar cycle favorable to certain drivers (see Figure 3).

The external and internal parts of the magnetic field disturbances at the IMAGE stations are derived using the Spherical Elementary Current System (SECS) method with two source layers of equivalent currents. The external current layer was placed at 90 km altitude, to represent all currents above, and the internal current layer at 1 m depth to represent all telluric currents (Juusola et al., 2020; Pulkkinen et al., 2003; Vanhamäki & Juusola, 2020). Poles of divergence-free SECSs were placed at these layers in the region covered by IMAGE, on uniform grids with 0.5° latitude and 1° longitude resolution. The amplitudes of the SECSs were determined by fitting their superposed magnetic field to the three components of the measured magnetic field. This separation is explained in further details in Section 2.2 of Juusola et al. (2023).

The amplitude of the time change of the external horizontal magnetic field disturbance was calculated as:

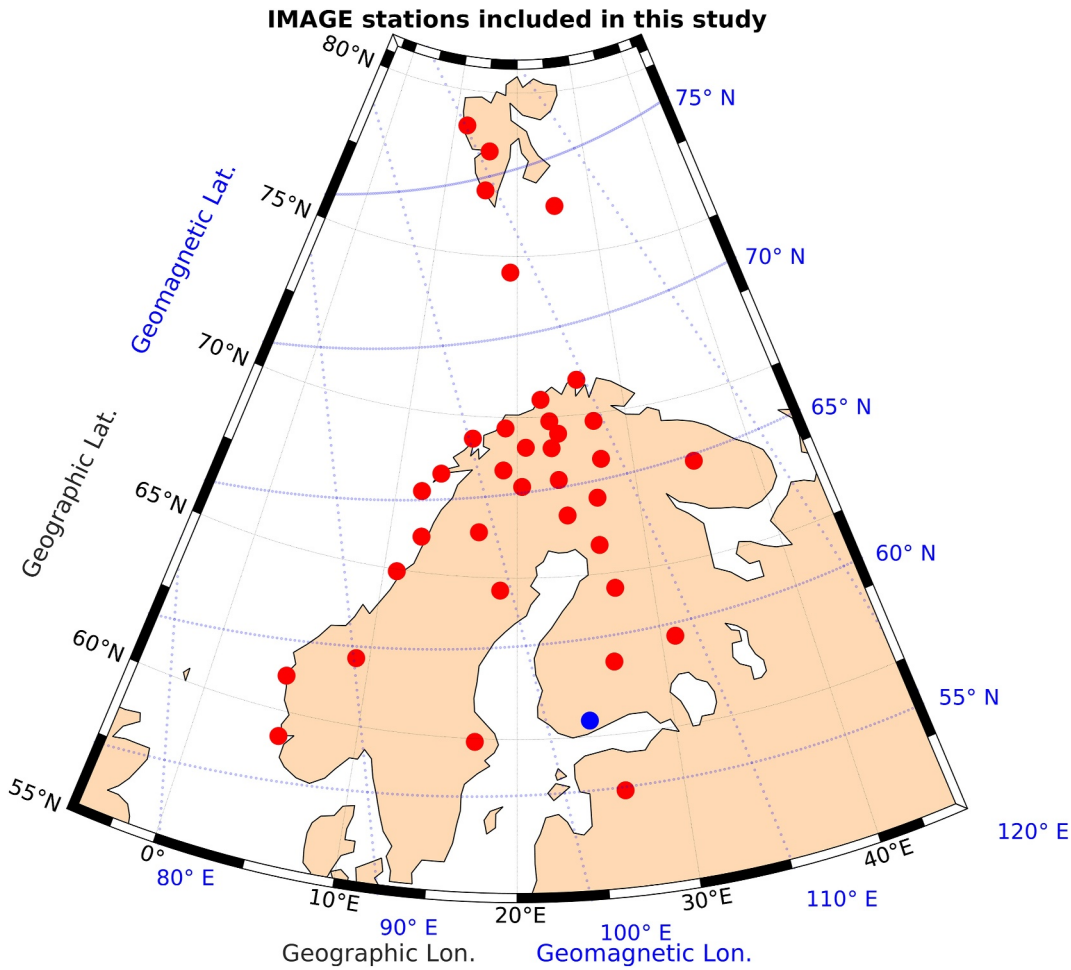

Figure 5. IMAGE magnetometer stations included in this study. To be included the station must be at a magnetic latitude above 54° MLAT and have at least 5 years of data. Nurmijärvi (NUR) station that was used in Figures 1 and 2 is shown by a blue circle. This figure was created using the M_Map mapping package for MatLab (Pawlowicz, 2020).

$$\left|\frac{d\boldsymbol{H}_{\text{ext}}}{dt}\right| = \sqrt{\left(\frac{d\Delta\boldsymbol{B}_{x,ext}}{dt}\right)^2 + \left(\frac{d\Delta\boldsymbol{B}_{x,ext}}{dt}\right)^2} \quad (1)$$

where $\Delta\boldsymbol{B}_{x,ext}$ and $\Delta\boldsymbol{B}_{x,ext}$ are the external north and east components of the magnetic field perturbation measured on the ground which are solely caused by ionospheric and magnetospheric currents. We use the notation $|d\boldsymbol{H}_{\text{ext}}/dt|$ because the time derivative is unaffected by the baseline subtraction applied to the field.

To avoid artificial jumps in the separated magnetic field, stations with missing data during a day have been discarded. Additionally, time derivatives exactly at midnight have been excluded from the analysis as artifacts may occur between days due to different station configurations (see Juusola et al., 2020, 2023). The internal $|d\boldsymbol{H}_{\text{ext}}/dt|$ could be calculated similarly but was not used in this study as we want to study the spatial and temporal evolution of rapid geomagnetic variations in the external component during storms. Figure 1 bottom panel shows $|d\boldsymbol{H}_{\text{ext}}/dt|$ at Nurmijärvi station (56.9° MLAT) with a dashed line indicating 0.5 nT/s.

To analyze the MLT distribution of large $|d\boldsymbol{H}_{\text{ext}}/dt|$ measurements versus development of the SSC, initial phase, main phase and recovery phases, the duration of each storm phase was separated into bins of equal percentage time for each storm. For each bin, we found all individual IMAGE magnetometer measurements with $|d\boldsymbol{H}_{\text{ext}}/dt|$ exceeding 0.5 nT/s. For the remainder of this paper, measurements exceeding 0.5 nT/s are called "spikes." Many studies have previously used 1 nT/s as a threshold for large $|d\boldsymbol{H}/dt|$ (e.g., Viljanen et al., 2001). When separating

into external and internal components more than half of the total $|d\boldsymbol{H}/dt|$ often comes from the internal part (see e.g. Juusola et al., 2020, 2023). When analyzing only the external component, 0.5 nT/s is a sufficiently high threshold and in line with previous studies.

In our statistical analysis presented in Section 3 the occurrence rate of spikes is normalized, so that probabilities can be calculated. The results are binned according to MLT and MLAT, or according to MLT and fractional duration of the storm phase, called the storm phase percentage (SPP). The total number of spikes in a given MLT-SPP bin, or MLT-MLAT bin, is divided by the total number of measurements in the bin, which yields the probability of spikes. In the supplementary material figures showing the total number of measurements inside each bin and figures showing the number of storms contributing to each bin are shown. The SSC bin is not on a percentage of the initial phase duration but covers the time from 2 min before the increase in SYM-H triggering the SSC to 5 min after to better capture the immediate impact of the magnetopause compression on the probability of spikes. The initial phase bins cover the time from the end of the SSC until the beginning of the main phase.

The results have been separated into the active solar wind driver at the time of the measurement, for example, if a part of one storm was driven by a sheath region that part contributes to the sheath category, while a later part of the same storm might contribute to the MC category. Because the strong solar wind-magnetosphere coupling that drives the storm terminates in the storm recovery phase, the storm recovery phase was limited to 24 hr and the driver of the storm recovery phase was prolonged so that the last active driver covers the remaining of the recovery phase up to 24 hr. This prolongation of the driver in the storm recovery phase only affects HSS/SIR and MCs, but not sheaths. A sheath is always followed by an ejecta or an MC and is therefore only the last active driver in the case it is ongoing at the end of the recovery phase or 24 hr into it. Figure 1 bottom panel shows how the end of the recovery phase MC driver was extended to the end of the storm recovery phase.

3. Statistics of Rapid Geomagnetic Variations

In this section we study the statistical occurrence of rapid geomagnetic variations in the external $|d\boldsymbol{H}_{ext}/dt|$ during the geomagnetic storms detected in Section 2.1 and categorized by the solar wind drivers identified in Section 2.2.

3.1. Temporal Evolution of Spikes During Geomagnetic Storms

This section investigates the distribution of spikes as function of MLT and scaled storm phase durations. This is accomplished by averaging the spike probabilities over all IMAGE stations covering 54°–78° MLAT that are located within the same 1 hr MLT and storm phase percentage (SPP) bin. In Section 3.2 the MLAT and MLT distribution of spike probabilities are investigated.

Figure 6 shows the probability of spikes ($|d\boldsymbol{H}_{ext}/dt| > 0.5$ nT/s) during the SSC, initial phase, main phase and recovery phase for the geomagnetic storms driven by different solar wind structures. The *x*-axis is the percentage of the initial phase (left), main phase (middle) and recovery phase (right) duration. The leftmost bin at the SSC is not on a percentage base but covers the time from 2 min before the positive jump in the SYM-H index to 5 min after. The normalization of probabilities is explained in Section 2.3.

According to Figure 6 the probabilities of spikes during the SSC in the grid cells in the 08–20 MLT sector are between 0.1 and 0.25 for HSS/SIR storms. This means that if there is an HSS/SIR-driven SSC ongoing, then 10%–25% of the time $|d\boldsymbol{H}_{ext}/dt|$ exceeds 0.5 nT/s in those grid cells in this MLT sector, as averaged over all the MLATs included (from 54° to 78° MLAT). The MLT sector is wider and probabilities are higher for sheath-driven storms, where three hotspots of high probabilities can be observed during the SSC, that is at 04–05, 08–11 and 14–17 MLT. For the MC-driven storms the statistics is sparse during the SSC, but enhanced probabilities are observed around 04–06 and 09–13 MLT. Few spikes are observed during the first half of the initial phase, with only slightly higher probabilities observed during MC and sheath-driven storms around 04–10 MLT. Low probabilities in the first half are expected, as it comprises the interval of time after the arrival of the shock to the solar wind coupling becoming intense enough to drive the geomagnetic storm. In the latter half of the initial phase, HSS/SIR-driven storms display some increase in the probabilities between 03 and 06 MLT, while sheath-driven storms display a slightly larger increase covering a wider region between 02 and 11 MLT.

For the storm main phase, shown in the middle column of Figure 6, HSS/SIR and MC-driven storms show a development with few occurrences at the beginning and increasing probabilities throughout the storm main phase, with maximum close to the SYM-H minimum. This is explained for MC-driven storms by the previous finding

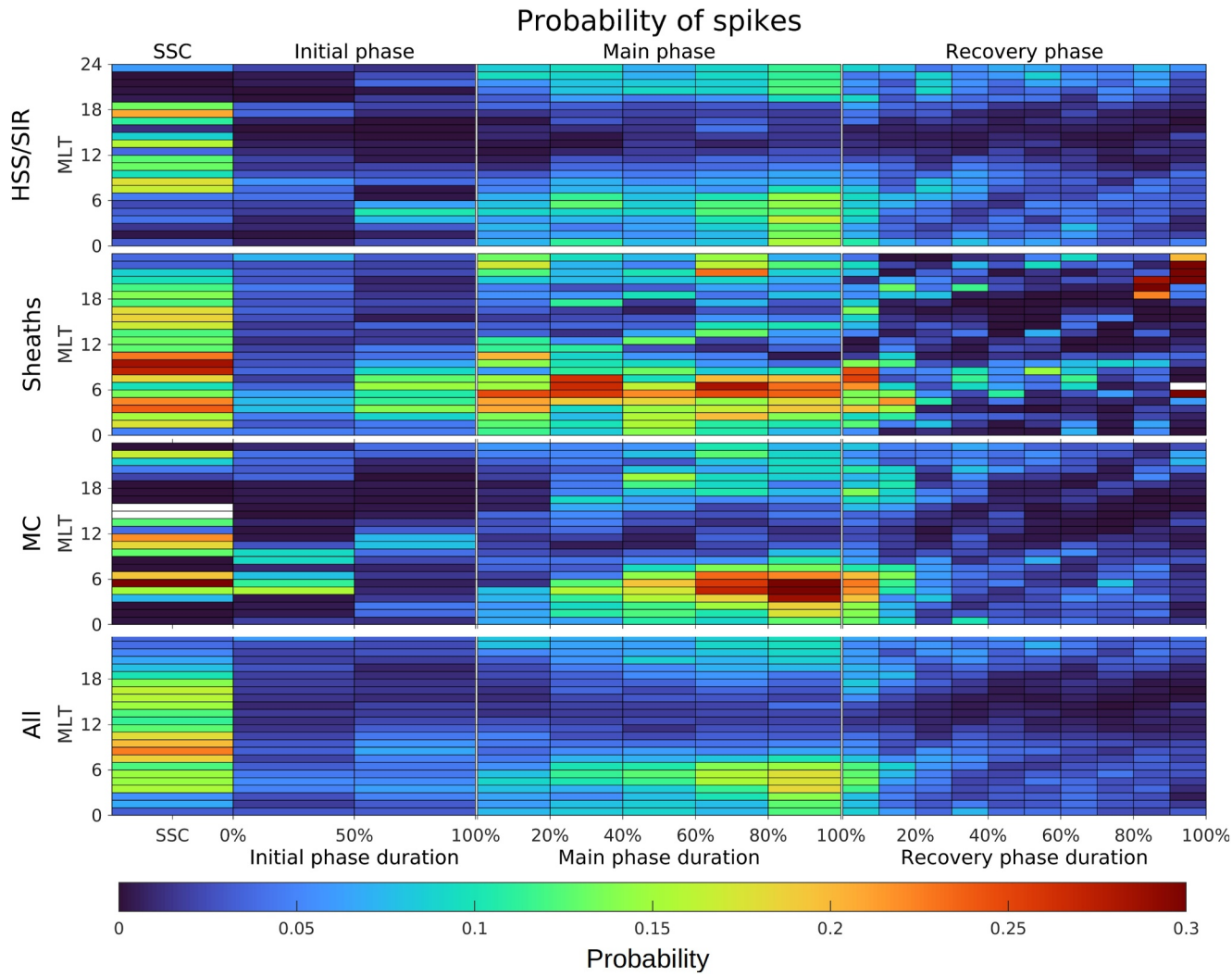

Figure 6. Probability of spikes in magnetic local time (MLT) and storm phase percentage (SPP) bins. Top shows HSS/SIR storms, middle top sheath storms, middle bottom MC storms and bottom all storms between 1996 and 2023. Left shows the SSC and initial phase, middle shows the main phase and right side shows the recovery phase. The bins have a size of 1 MLT hr and the SPP are of size 50% of the phase duration for the initial phase, 20% for the main phase and 10% for the recovery phase. At 100% of the initial phase begins the main phase, and at 100% of the main phase begins the recovery phase. The SSC bins are 10 min and cover the time from 2 min before the jump in the SYM-H index to 5 min after.

that they have field-aligned and ionospheric equivalent currents that develop gradually and maximize close to the end of the main phase (see Figure 9 in Pedersen et al., 2022). However, in HSS/SIR-driven storms the currents develop faster during the geomagnetic storm and the largest currents that typically cause spikes have been reported early in the storm main phase (Pedersen et al., 2021). The fact that Pedersen et al. (2021) used clock time, and did not scale the storm phases like in Figure 6 appears to account for some of this discrepancy. If the analysis in Pedersen et al. (2021) is repeated by re-scaling the main phase in the same way as in the present study, then the second peak in the superposed total ionospheric and field-aligned currents in their Figure 4 becomes equally large as the first, which may explain some of the high probabilities for spikes close to the end of the storm main phase.

The MLT regions of the spikes in HSS/SIR storms also extend as the main phase progresses, starting with two distinct peaks, one in the pre-midnight sector and one in the morning sector, that at the end of the main phase overlap through the midnight region. On the other hand, sheath-driven storms show a high probability for spikes throughout the entire storm main phase, with two distinct peaks in the pre-midnight and morning sectors. The largest extent in MLT is seen at the beginning of the storm main phase, where high probabilities can be seen from 20 to 13 MLT. The morning sector region slightly contracts toward the mid and late main phase, where it only

reaches 9 MLT. This is in agreement with the evolution and extent of large ionospheric and field-aligned currents (FAC) during the main phase of sheath-driven storms, where the currents develop quickly and reach the largest extent early, while they remain large throughout the entire storm main phase (Pedersen et al., 2022).

The probability of spikes quickly decreases during the storm recovery phase, shown in the right column of Figure 6. For the first 20% of the recovery phase, the probability decreases from 0.25 to less than 0.1 in the morning sector of sheath and MC-driven storms. For HSS/SIR storms elevated probabilities of spikes of 0.05–0.1 are observed throughout the entire storm recovery phase in parts of the morning and particularly pre-midnight sectors. For sheath-driven storms, some occasions of higher probabilities are seen during the middle of the recovery phase, particularly in the morning sector. At the very end of sheath-driven storms, in the bins 80%–100% of the recovery phase in the pre-midnight sector, high probabilities of >0.3 are seen. It should be noted that very few sheaths were active during the end of the storm recovery phase, as the solar wind at Earth transitions into the ICME ejecta or MC (figures of total number of points and storms contributing to each bin are in the supplementary material). Those bins with very high probability at the end of the recovery phase are highly influenced by the activity of just a few storms, in particular the "second" Halloween storm on the 30th of October 2003 that was driven by the sheath of a new ICME as can be seen in Figure 2. The onset of the "second" Halloween storm is chosen according to the storm detection algorithm in Section 2.1.1 at the most positive SYM-H value between the two storms, which for this storm had large ionospheric disturbances prior to it.

The bottom panel includes all storms from 1996 to 2023, that is, also storms where the interplanetary driver was not identified in Section 2.2. The highest probabilities of spikes are seen during the SSC and the storm main phase. For the typical storm, at the beginning of the storm main phase the probability for spikes is 0.09 between 23 and 01 MLT and between 04 and 05 MLT. As the main phase progresses the probabilities increase and the MLT extent of the two regions widens. Toward the end of the storm main phase, the region with spike probabilities higher than 0.09 has extended to 21-08 MLT, with the highest probability of 0.18 in the morning region between 03 and 06 MLT.

3.2. Spatial Evolution of Spikes During Geomagnetic Storms

In this section we study the MLT-MLAT distribution of spikes during each storm phase. In contrast to Section 3.1, here the reported probabilities of spikes are averaged over the storm phase but not over MLAT. This section offers a complementary view to Section 3.1 of the full three dimensional MLT-MLAT-storm phase distribution of spikes during geomagnetic storms.

Figure 7 shows the MLT-MLAT distribution of spike probabilities during the SSC, main phase and recovery phase as viewed from above the north geomagnetic pole in altitude adjusted corrected geomagnetic (AACGM) coordinates (Baker & Wing, 1989). The initial phase (after the SSC and before the main phase) is not shown because of the long intervals of little activity.

During the SSC, shown in the left column of Figure 7, HSS/SIR storms have an increased spike probability on the dayside from 7 to 19 MLT. For sheath-driven storms, which are responsible for by far the most SSCs, the region of high probabilities above 0.10 is vastly larger than for HSS/SIR storms, extending from 02 to 22 MLT. Three MLT hotspots can be observed during the sheath-driven SSCs, in the post-midnight at 03–04 MLT, in the pre-noon from 07 to 11 MLT and in the afternoon from 14 to 17 MLT. Only the pre-noon SSC hotspot extends into the polar region, where probabilities exceeding 0.3 are seen above 70° MLAT as well. The MLT extent of spikes in the polar region is narrower than that of the mainland stations and typically increased probabilities are seen between 3 and 18 MLT for sheath-driven storms. The divide between the mainland and polar stations is visible in all figures around 70° MLAT where there is a gap of IMAGE stations.

During the main phase, shown in the middle row of Figure 7, the highest probabilities are seen in the morning sector for all storm drivers. The activity of large $|d\boldsymbol{H}_{ext}/dt|$ in this sector is most likely associated with omega bands (e.g., Apatenkov et al., 2020; Juusola et al., 2015, 2023; Milan, Imber, et al., 2023). The MLT extent of the morning region hotspot is the largest for sheath-driven storms, where probabilities >0.20 extend from 03 to 08 MLT over the MLAT range 63°–67.5°. The highest probabilities of 0.48 are found between 06 and 08 MLT at the high-latitude mainland stations 65°–67.5° MLAT. The latitudinal extent is similar for MC-driven storms, although the MLT width is slightly narrower, only extending from 03 to 07 MLT for probabilities >0.20. Only sheath-driven storms have spikes extending beyond noon, which might be related to the high solar wind dynamic

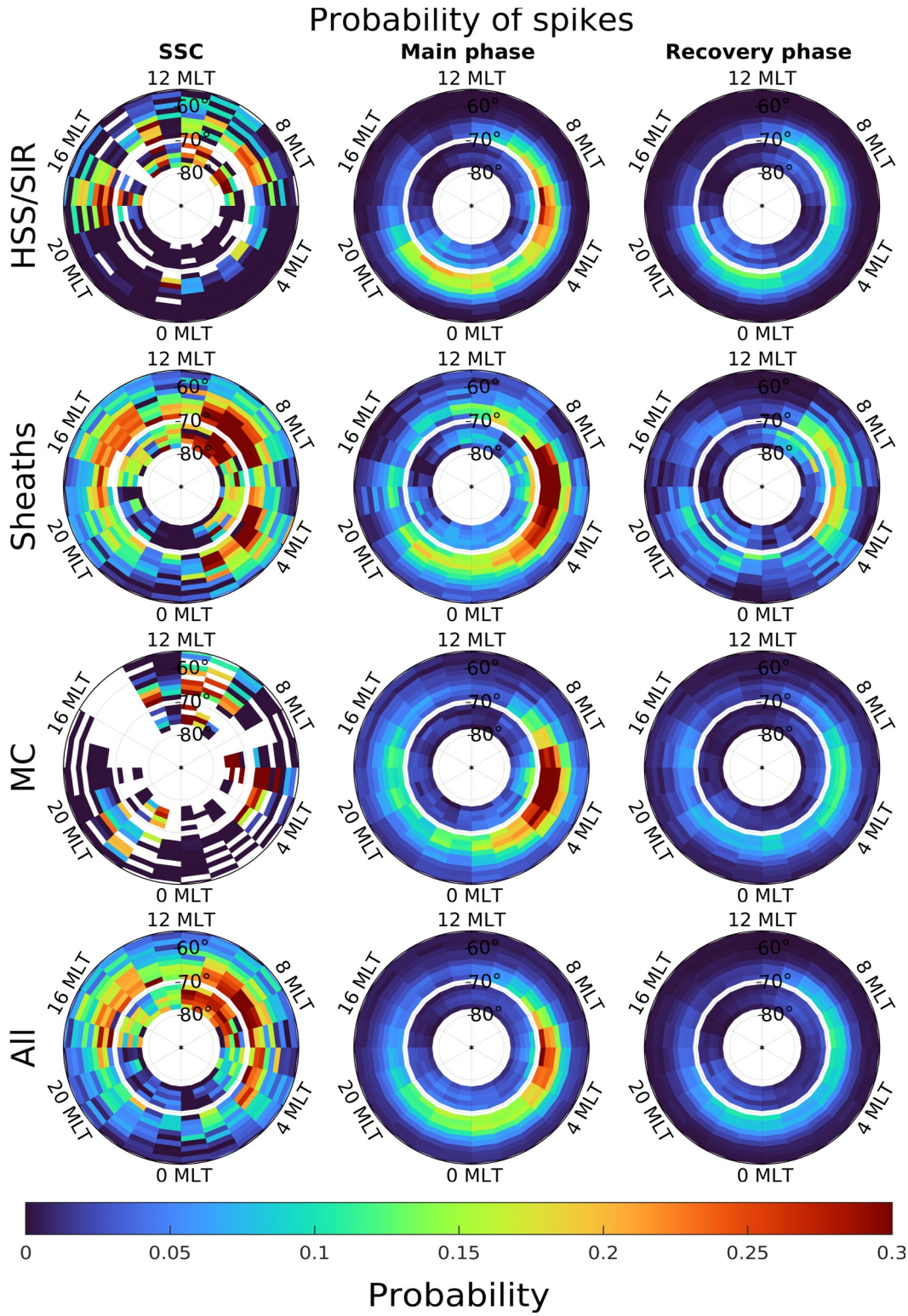

Figure 7. Probability of spikes in magnetic local time (MLT) and magnetic latitude (MLAT). From the top to bottom row are the HSS/SIR storms, sheath storms, MC storms and in the bottom are all geomagnetic storms from 1996 to 2023. The left side is at the SSC, the middle is during the storm main phase, and the right is during the storm recovery phase. The bins are of size 1° MLT hour and 1.5° in MLAT. The lower limit MLAT bins is at 54° and the higher limit is at 78°.

pressure during the passage of sheaths (e.g., Kilpua et al., 2017). Throughout all MLTs, the probability of spikes is lower in the polar region than for the mainland stations, and only slightly increased probabilities are seen extending into the polar latitudes around 06 MLT.

A second distinct MLT hotspot was seen in the pre-midnight region during the beginning of the main phase in Figure 6 for HSS/SIR and MC storms, and occasionally for sheath storms. However, when analyzing the whole main phase as in Figure 7, the pre-midnight hotspot disappears for sheath and MC storms. It stands out and has the highest probabilities out of the storm categories for HSS/SIR storms around 21–23 MLT at 67° MLAT, with some patches of elevated probabilities extending into the polar region. The spikes in the pre-midnight region have been shown to be associated with substorm onsets and westward traveling surges (Juusola et al., 2015; Milan, Imber, et al., 2023; Schillings et al., 2022). However, for the ICME sheath and MC storms elevated probabilities are seen arising around 18 MLT, which is not visible for HSS/SIR storms.

The right column of Figure 7 shows that spike probabilities drastically decrease for all drivers in the recovery phase compared to the SSC and main phase, and different regions and latitudinal extents are prominent depending on the geomagnetic storm driver. The pre-midnight hotspot becomes more distinct during the storm recovery phase, and particularly for HSS/SIR-driven storms where it has equally high probabilities as the morning region hotspot. For sheath and MC-driven storms the morning hotspot is still the most dominant. Sheath storms have the highest probabilities of spikes and largest extent in both MLT and MLAT in the morning sector, and interestingly, sheath-driven storms have an increased probability for spikes in the pre-noon polar region—as was also seen during the SSC. This polar region is the most noon-ward extent of the spikes in the recovery phase.

4. Discussion

4.1. About the Methodology

The results in Figures 6 and 7 are very robust to changes in the threshold value and methods of counting spikes. In these figures we show all spikes larger than 0.5 nT/s without any form of filtering. However, we tested various ways of filtering the number of spikes to limit the influence of a few large storms that have a long-lasting series of $|d\boldsymbol{H}_{ext}/dt|$ values exceeding the threshold value by filtering the spikes into events that had to be separated by 30, 120 and 600 s. Filtering the spikes like this did not have a large impact on the distribution of spikes seen in Figures 6 and 7, but made the definition and meaning of the probabilities less straightforward. We also repeated the analysis for many different threshold values to see how that affected the results. The same distributions of spikes emerged for higher threshold values, only the probabilities became lower. This demonstrates that the distributions are very robust to changes in methodology.

The importance of removing the internal component that contributes to $|d\boldsymbol{H}/dt|$ should be emphasized when studying the statistical behavior of geomagnetic variations during geomagnetic storms. Geomagnetic storms have a UT dependence, with the Dst or SYM-H index minima most frequently occurring around 06–08 and 21–23 UT (see e.g. Balan et al., 2021, and Figure S1 in Supporting Information S1). A UT dependence has also been reported for sudden commencement (Zhou & Lühr, 2022). The internal component makes up a large part of the total measured $|d\boldsymbol{H}/dt|$ (cf. Table 2 in Juusola et al., 2020). The contribution of the internal component depends on location due to the spatial variation in ground conductivity. Therefore, when showing the distribution of spikes from selected stations as function of MLT, like in Figures 6 and 7, the UT dependence together with the local ground conductivity structures could bias the result. This bias can be eliminated by only considering the external component.

4.2. Spikes During SSC

Several studies have reported large GICs during SSCs, particularly at low and mid-latitudes (e.g., Zhang et al., 2015; Smith et al., 2021; Marshall et al., 2022, and references therein). The largest hotspot during SSC seen in Figure 7 occurs in the pre-noon sector between 07 and 11 MLT, extending to 12 MLT above 70° MLAT for sheaths and all storms. Traveling convection vortices (TCVs) in the high-latitude geomagnetic field perturbations have been observed following rapid dayside compression of the magnetosphere because of sudden changes in the solar wind (Friis-Christensen et al., 1988). TCVs have their center and largest magnetic field perturbations at ~73°–75° MLAT, occur most frequently at 08–10 MLT and have a typical horizontal size of 1,000–3,000 km (~2–7 MLT hr) (see e.g. Glassmeier et al., 1989; Amm et al., 2002; H. Kim et al., 2017). The

region and extent of TCVs following pressure pulses in the solar wind coincide with the pre-noon SSC hotspot, especially in the polar region. TCV could be a possible mechanism, together with Kelvin Helmholtz instabilities, that drives spikes in this SSC hotspot.

A post-midnight SSC hotspot occur at 04 MLT. By inspecting individual events where spikes are seen in the nightside during the SSC, the spikes and the post-midnight hotspot seem to occur if IMF B_Z is southward at the time of the SSC and there are already large currents present. This could be a result of compression of the entire magnetosphere that enhances already existing currents that give rise to large $|d\boldsymbol{H}_{ext}/dt|$. This hotspot is only seen for ICME storms. For HSS/SIR storms, low probabilities of spikes are seen throughout the entire nightside during SSCs.

The MLAT extent of the high probability spikes during the SSC is wider than during the main phase and recovery phase as seen in Figure 7, extending down to the lower MLAT limit of 54° in the pre-noon and post-noon hotspot for sheaths and all storms. It is apparent that during the SSC, spikes are likely to occur in different regions than during the main and recovery phases of geomagnetic storms. These observations suggest that those three (two) hotspots during the passage of ICME sheaths (HSSs/SIRs) warrant extra precautions during the early arrival of these interplanetary structures likely to cause SSCs.

4.3. MLT and MLAT Extent of Spikes During Main and Recovery Phases

It is clear that the evolution of spikes throughout the storm main phase depends on the solar wind driver. Storms with main phases driven by HSS/SIR and MCs have a gradual increase in the probability of spikes which maximizes toward the end of the main phase, while storms driven by sheaths have a high probability of spikes throughout the entire main phase. This agrees with the finding of Huttunen et al. (2008) that sheath storms can cause large GICs even when no activity is seen in the Dst index, while this is not the case for GICs by the ejecta. This can be explained by the turbulent structure of sheaths where strong solar wind-magnetospheric coupling is more likely to occur suddenly and at any time throughout the storm main phase.

The MLT extent of the region where spikes occur with probability higher than 0.15 during the storm main phase, as seen in Figure 7, is 20–11 MLT for sheaths, 20-09 MLT for HSS/SIR and 00–08 MLT for MC-driven storms. Figures 6 and 7 clearly show that MCs are an equally big threat with regards to large $|d\boldsymbol{H}_{ext}/dt|$ in the morning sector during the main phase of geomagnetic storms as sheaths. MCs are very coherent interplanetary structures with autocorrelation functions of solar wind parameters and ionospheric currents decaying much slower than for HSS/SIR and sheaths (Pedersen et al., 2023). This shows that large $|d\boldsymbol{H}_{ext}/dt|$ in the morning sector also take place during steady solar wind coupling. However, the coherent MC structures are less likely to cause pre-midnight spikes than the denser and more turbulent HSS/SIR and sheaths. The MLAT region of spike probabilities higher than 0.15 is the widest for sheath and MC-driven storms, covering the latitudes from 60° to 67.5°. HSS/SIR-driven storms have a narrower extent in MLAT of spike probabilities higher than 0.15, extending from 63° to 67.5° MLAT. There is a gap in the data coverage between the IMAGE mainland stations at 67.5° and polar stations at 71.4° MLAT, which results in uncertainties of the higher latitude boundaries.

During the storm main phase, Figure 7 showed two distinct hotspots for HSS/SIR storms, while for sheath and MC-driven storms the morning hotspot completely dominates. Milan, Imber, et al. (2023) showed that the morning sector spikes in SuperMAG data were almost completely absent during the quiet year of 2008, which was a year with no ICME-driven storms (see Figure 3). Although HSS/SIR-driven storms have a lower probability of spikes than sheath and MC-driven storms, they are still responsible for the majority of spikes during the solar cycle because of their high occurrence rate. It was reported by Milan, Imber, et al. (2023) that the occurrence of $|dB/dt| > 300$ nT/min in SuperMAG data peaked during the declining phase of the solar cycle, when HSS/SIR storms are most frequent.

It is interesting that HSS/SIR-driven storms have so pronounced increases in probability in the pre-midnight region of the main and recovery phase seen in Figures 6 and 7. The HSS/SIR storms contain Alfvénic fluctuations embedded in the HSS that cause high-intensity long-duration continuous AE activity (HILDCAA) (Guarnieri et al., 2007). Controversy exists about whether HILDCAA during the recovery phase of HSS/SIRs is related to substorm occurrences, which is the primary cause of geomagnetic variation in the pre-midnight region (Tsurutani et al., 2004, 2006; H.-J. Kim et al., 2008). Be that as it may, Milan, Mooney et al. (2023) studied HSS/SIR with HILDCAA events and also observed spikes in the pre-midnight region and stated that this type of

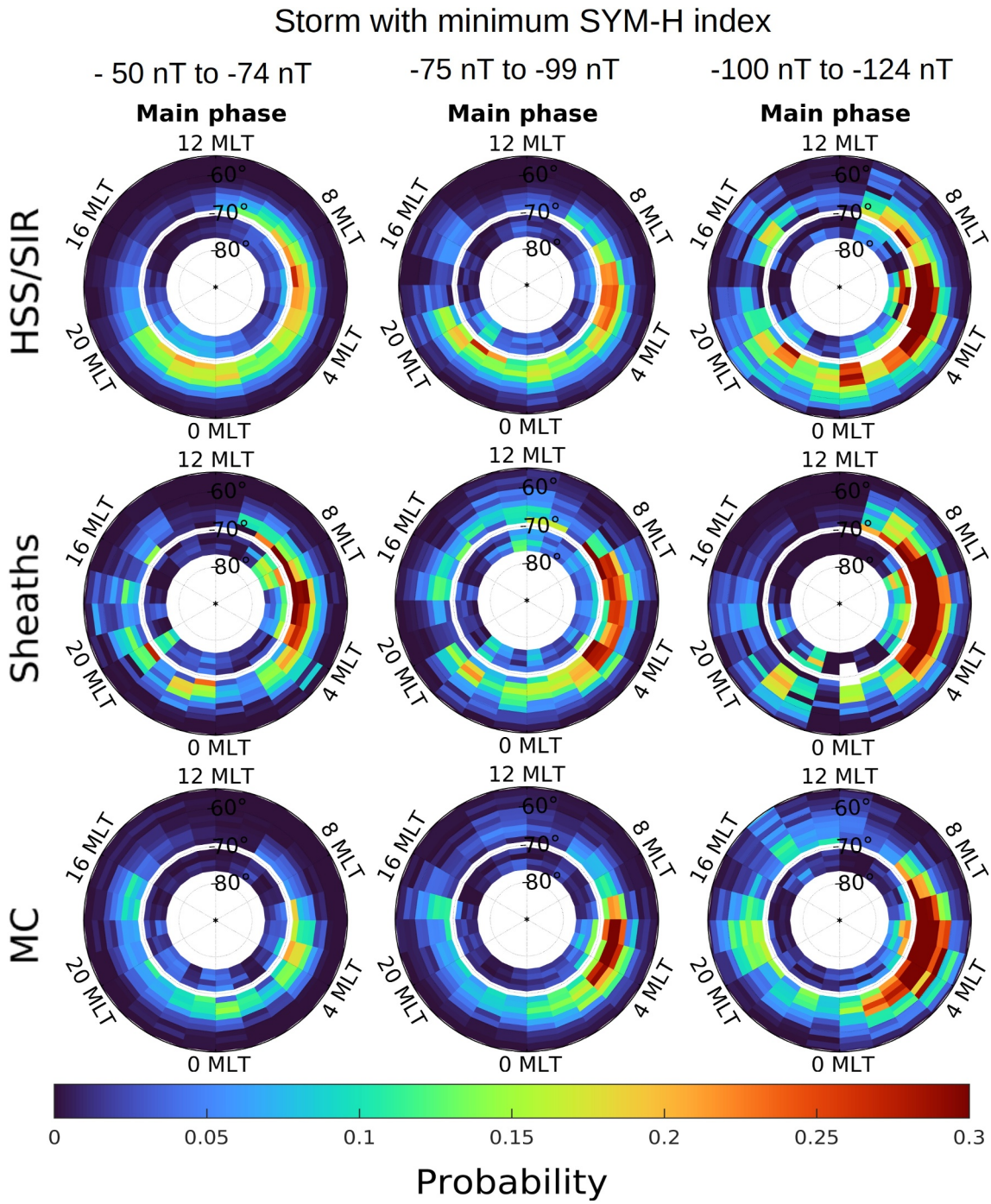

Figure 8. Probability of spikes in magnetic local time (MLT) and magnetic latitude (MLAT) for the main phase during storms separated by storm intensity. The left column is storms with a minimum SYM-H index between −50 and −74 nT. The middle column are storms between −75 and −99 nT, and the right column are storms between −100 and −124 nT.

activity is sufficient to pose a significant risk of GICs. This is in agreement with Engebretson et al. (2024) observation that extreme geomagnetic disturbances in Arctic Canada at latitudes between 65° and 70° were associated with high-speed solar wind streams and occurred during the declining phase of the solar cycle.

Schillings et al. (2022) reported that during geomagnetic storms the location of spikes develops from the pre-midnight sector to the morning sector. The results by Schillings et al. (2022) might explain why the morning sector probabilities seen in Figure 6 maximize immediately after the pre-midnight probabilities for sheath and MC-driven storms. Sheath storms have the highest probabilities in the pre-midnight sector at $0-20\%$ and $60-80\%$ of the main phase duration, and the morning sector has the highest probabilities in $20-40\%$ and at the end of the main phase. Likewise, for MC-driven storms the pre-midnight sector maximizes when the main phase is at $60-80\%$ and the morning sector at $80-100\%$ of the duration.

4.4. Effect of Storm Intensity

It is well known that HSSs/SIRs drive weaker storms than ICMEs (e.g., Borovsky & Denton, 2006). Figure 4 shows that the majority of the HSS/SIR-driven storms do not reach SYM-H index below −75 nT, and none below −137 nT (see Table 1). In contrast, ICME-storms have a substantial fraction of intense storms with SYM-H index below −150 nT. This poses the question of whether similarly sized HSS/SIR, sheaths and MC-driven storms are equally effective at causing spikes. Figure 8 shows the probability of spikes for HSS/SIR, sheath and MC-driven storms separated by minimum SYM-H index. It can be seen that weaker storms have a lower probability of spikes and narrower extent in MLT and MLAT compared to more intense storms. In the storm category for minimum SYM-H index between −100 and −124 nT, HSS/SIR-driven storms have almost equally high probability of spikes in the morning region as ICME sheath and MC-driven storms. This shows that the relatively low probability of spikes seen in Figures 6 and 7 during HSS/SIR-driven storms compared to ICME-driven storms comes from the fact that HSS/SIR-driven storms are responsible for many more weak-to-moderate sized storms. However, in the midnight sector and at the pre-midnight hotspot the probability of spikes is typically higher for HSS/SIR-driven storms compared to equally strong sheath or MC-driven storms.

4.5. Forecasting Spikes in $|\mathrm{d}\boldsymbol{H}_{\mathrm{ext}}/\mathrm{d}t|$

Observations of halo CMEs heading toward Earth (e.g., Robbrecht & Berghmans, 2004; Webb & Howard, 2012) or coronal holes as the source of HSS/SIR on the Sun can give us an early indication of the type of interplanetary structure that may impact Earth's environment in the coming days. This study has characterized the spatial extent of rapid geomagnetic variations above 54° MLAT during geomagnetic storms following the arrival of these interplanetary structures. The results of this study can help us forecast when geomagnetic storms are most likely to cause spikes in $|\mathrm{d}\boldsymbol{H}_{\mathrm{ext}}/\mathrm{d}t|$ and in which MLT/MLAT region those spikes are likely to occur.

Figure 9 illustrates the progression of geomagnetic storms and the regions with high and very high probability of spikes in $|\mathrm{d}\boldsymbol{H}_{\mathrm{ext}}/\mathrm{d}t|$ following the arrival of HSS/SIR and ICMEs. The regions with high probability of spikes implies a probability $P > 0.20$ for the SSC, $P > 0.15$ for the main phase (MP) or $P > 0.10$ for the recovery phase (RP), and very high probability of spikes implies $P > 0.30$ for SSC or $P > 0.25$ for MP. It typically takes between 1 and 5 days for the solar wind from a coronal hole or CME to reach Earth's orbit (Richardson & Cane, 2010). For extreme cases this transit time can be even faster, such as for the July 2012 CME that reached 1 AU within 21 hr (Cash et al., 2015).

The chance for a SSC to occur is highest at the initial impact of the solar wind structure upon the magnetopause. At that time attention should be paid to the two (for HSS/SIR) or three (for ICMEs) SSC hotspots. The two ICME hotspots at 04 and 09 MLT have very high probability for spikes. During the storm main phase spikes occur from the morning to midnight sector, regardless of the driver. ICME driven storms have regions of very high probability, which are all concentrated in the morning sector. Spikes still occur during the recovery phase, but with lower probability and extent than during the main phase.

5. Conclusions

This paper presents an automated algorithm for identifying geomagnetic storms and storm phases. A catalog of 755 geomagnetic storms and the storm phases with interplanetary drivers from January 1996 to June 2023 is provided as supplementary material. Using those storms and IMAGE ground magnetometer 10 s resolution data,

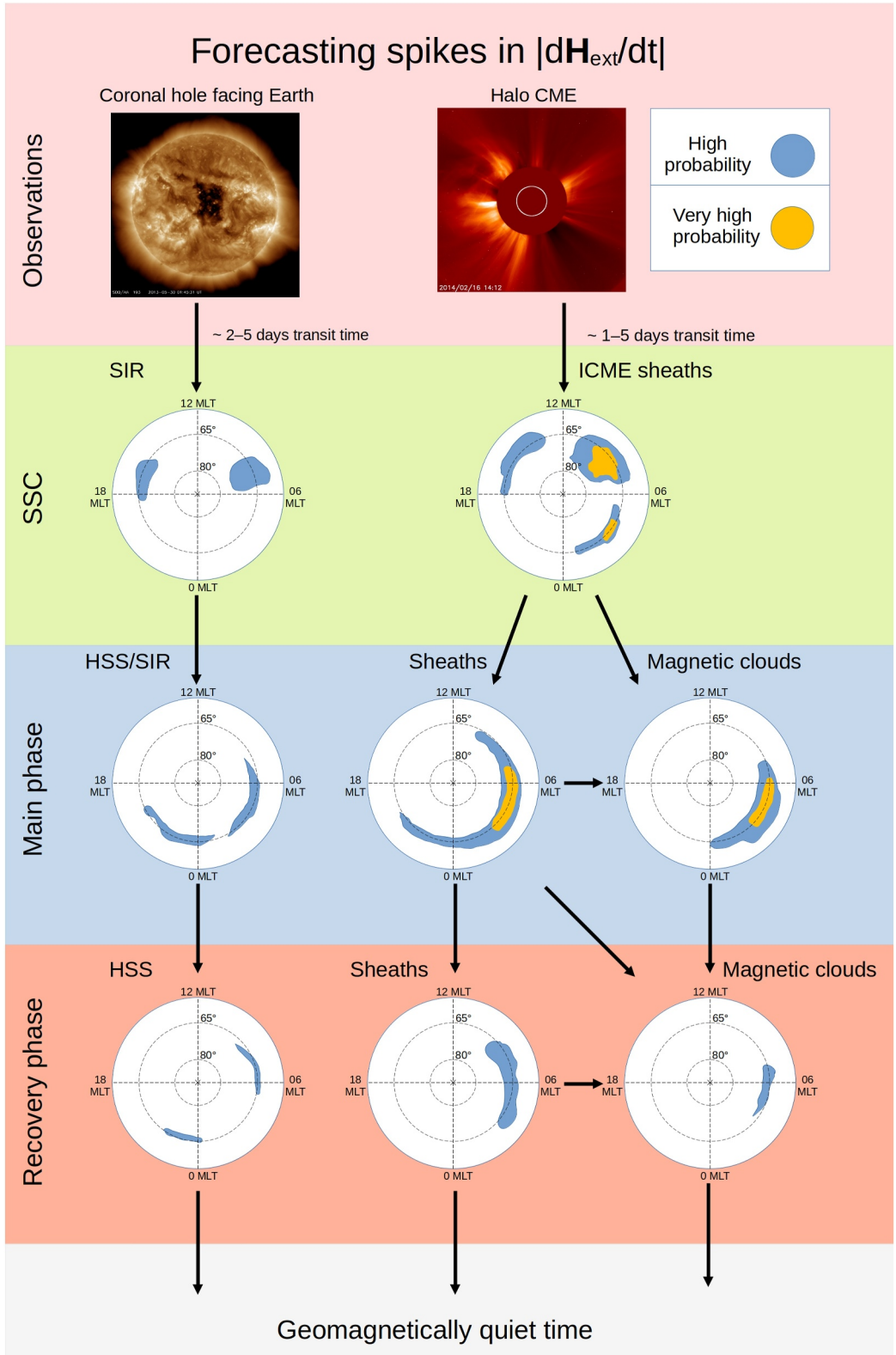

Figure 9. Schematic illustrating the regions as viewed from above the north geomagnetic pole in aacgm coordinates with high and very high probability of spikes during the SSC, main phase and recovery phase for storms driven by HSS/SIR, sheaths and magnetic clouds. The two images in the top show a coronal hole and a halo CME taken by the Solar Dynamics Observatory and the Solar and Heliospheric Observatory, respectively.

it has been shown that both the temporal and spatial development and extent of rapid geomagnetic variations in the external (caused by ionospheric and magnetospheric currents) $|d\boldsymbol{H}_{ext}/dt| > 0.5$ nT/s, denoted as *spikes*, is characterized by the geomagnetic storm driver.

The following key points summarize the main results of this study.

- HSS/SIRs are responsible for 67% of all storms with minimum SYM-H index in the range −50 to −74 nT, and 40% of storms in the range of −75 to −99 nT. ICMEs are responsible for all storms with a minimum SYM-H index of less than −137 nT between January 1996 and June 2023.
- For all three storm drivers, the highest probabilities of spikes during the storm main phase are seen in the morning sector centered around 05 MLT.
- The probability for spikes gradually increases from ∼0.08 in the morning sector at the beginning of the storm main phase to 0.16 and 0.30 at the end of the storm main phase for HSS/SIR and MC-driven storms, respectively. On the contrary, sheath-driven storms have probabilities of ∼0.25 in the morning sector throughout the entire storm main phase.
- Sheath storms have the widest MLT extent of spikes during the storm main phase with probabilities higher than 0.15 extending from 19 to 11 MLT. For HSS/SIR storms the extent is from 19 to 09 MLT and MC-driven storms 00–08 MLT. Storms driven by MCs (coherent solar wind structures) pose an equally large risk of spikes in the morning region as sheaths (turbulent structures), but fewer spikes in the pre-midnight region associated with substorms than sheaths or HSS/SIR.
- Sheath and MC-driven storms have the widest MLAT extent of spikes with probabilities higher than 0.15 during the storm main phase extending from 60° to 67.5° MLAT, while HSS/SIR storms the MLAT extent is narrower extending from 63° to 67.5° MLAT.
- HSS/SIR storms cause more pre-midnight spikes than ICME storms. Elevated probabilities of pre-midnight spikes are also seen throughout the entire recovery phase for HSS/SIR storms. This is likely related to HILDCAA in the HSS storm recovery phase, causing intermittent reconnection due to the Alfvén fluctuations in the IMF.
- Three MLT hotspots are observed related to the SSC. These are in the post-midnight at 04 MLT, pre-noon at 09 MLT, and afternoon at 15 MLT and occur within 10 min of the SSC. The pre-noon hotspot has the highest probability of spikes and extends well into the polar region up to 78° MLAT.
- Spikes occur over a wide MLAT range during SSCs, reaching lower latitudes than during the main or recovery phase. Probabilities greater than 0.15 extend down to the lower MLAT limit of 54°.
- Finally, the fact that HSS/SIR storms have a lower probability of spikes in the morning sector than ICME storms during the main phase seems to arise because HSS/SIR are limited to producing mainly weak-to-moderate storms. The intensity of the storm in terms of the SYM-H index plays a role in the probability of spikes during the main phase. For storms with similar SYM-H minima, HSS/SIR-driven storms have about equally high probabilities of spikes in the morning sector than ICME sheath and MC-driven storms.

Data Availability Statement

All the data used in this study can be freely downloaded from the world wide web. The catalog of geomagnetic storms, their phases and interplanetary drivers are attached as supplementary material to this article. The MATLAB package developed to detect geomagnetic storms and storm phases described in this article is available at Pedersen et al. (2024). The IMAGE magnetometer data can be accessed from https://space.fmi.fi/image. The SYM-H index can be downloaded from the WDC for Geomagnetism, Kyoto University at https://wdc.kugi.kyoto-u.ac.jp/aeasy/index.html. The solar wind and interplanetary field data from OMNIWeb can be downloaded from https://omniweb.gsfc.nasa.gov/form/omni_min_def.html. The ICME catalog is available at Richardson and Cane (2024) and the HSS/SIR catalog in Grandin et al. (2019).

References

Ahmed, O., Badruddin, B., & Derouich, M. (2024). Characteristics and development of the main phase disturbance in geomagnetic storms (Dst ⩽ −50 nT). *Advances in Space Research*, *73*(9), 4453–4481. https://doi.org/10.1016/j.asr.2024.01.050

Amm, O., Engebretson, M., Hughes, T., Newitt, L., Viljanen, A., & Watermann, J. (2002). A traveling convection vortex event study: Instantaneous ionospheric equivalent currents, estimation of field-aligned currents, and the role of induced currents. *Journal of Geophysical Research*, *107*(A11), SIA–1. https://doi.org/10.1029/2002JA009472

Acknowledgments
This work was supported by the Vilho, Yrjö and Kalle Väisälä Foundation and Academy of Finland projects 354521, 348782 and 339329. For the geomagnetic indices, solar wind and interplanetary magnetic field data we gratefully thank NASA/GSFC's Space Physics Data Facility's OMNIWeb (https://omniweb.gsfc.nasa.gov/). We thank the institutes who maintain the IMAGE Magnetometer Array: Tromsø Geophysical Observatory of UiT the Arctic University of Norway (Norway), Finnish Meteorological Institute (Finland), Institute of Geophysics Polish Academy of Sciences (Poland), GFZ German Research Centre for Geosciences (Germany), Geological Survey of Sweden (Sweden), Swedish Institute of Space Physics (Sweden), Sodankylä Geophysical Observatory of the University of Oulu (Finland), Polar Geophysical Institute (Russia), DTU Technical University of Denmark (Denmark), and Science Institute of the University of Iceland (Iceland). The provisioning of data from AAL, GOT, HAS, NRA, VXJ, FKP, ROE, BFE, BOR, HOV, SCO, KUL, and NAQ is supported by the ESA contracts number 4000128139/19/D/CT as well as 4000138064/22/D/KS.

Apatenkov, S., Pilipenko, V., Gordeev, E., Viljanen, A., Juusola, L., Belakhovsky, V., et al. (2020). Auroral omega bands are a significant cause of large geomagnetically induced currents. *Geophysical Research Letters*, *47*(6), e2019GL086677. https://doi.org/10.1029/2019GL086677

Baker, K., & Wing, S. (1989). A new magnetic coordinate system for conjugate studies at high latitudes. *Journal of Geophysical Research*, *94*(A7), 9139–9143. https://doi.org/10.1029/ja094ia07p09139

Balan, N., Ram, S. T., Manu, V., Zhao, L., Xing, Z.-Y., & Zhang, Q.-H. (2021). Diurnal ut variation of low latitude geomagnetic storms using six indices. *Journal of Geophysical Research: Space Physics*, *126*(10), e2020JA028854. https://doi.org/10.1029/2020JA028854

Balan, N., Tulasiram, S., Kamide, Y., Batista, I. S., Souza, J. R. d., Shiokawa, K., et al. (2017). Automatic selection of dst storms and their seasonal variations in two versions of dst in 50 years. *Earth Planets and Space*, *69*, 1–11. https://doi.org/10.1186/s40623-017-0642-2

Blagoveshchensky, D., & Sergeeva, M. (2019). Impact of geomagnetic storm of september 7–8, 2017 on ionosphere and hf propagation: A multi-instrument study. *Advances in Space Research*, *63*(1), 239–256. https://doi.org/10.1016/j.asr.2018.07.016

Bolduc, L., Langlois, P., Boteler, D., & Pirjola, R. (1998). A study of geoelectromagnetic disturbances in quebec. i. general results. *IEEE Transactions on Power Delivery*, *13*(4), 1251–1256. https://doi.org/10.1109/61.714492

Borovsky, J. E., & Denton, M. H. (2006). Differences between cme-driven storms and cir-driven storms. *Journal of Geophysical Research*, *111*(A7). https://doi.org/10.1029/2005ja011447

Bothmer, V., & Schwenn, R. (1995). The interplanetary and solar causes of major geomagnetic storms. *Journal of Geomagnetism and Geoelectricity*, *47*(11), 1127–1132. https://doi.org/10.5636/jgg.47.1127

Burton, R. K., McPherron, R., & Russell, C. (1975). An empirical relationship between interplanetary conditions and dst. *Journal of Geophysical Research*, *80*(31), 4204–4214. https://doi.org/10.1029/JA080i031p04204

Cane, H., & Richardson, I. (2003). Interplanetary coronal mass ejections in the near-earth solar wind during 1996–2002. *Journal of Geophysical Research*, *108*(A4). https://doi.org/10.1029/2002JA009817

Cash, M., Biesecker, D., Pizzo, V., de Koning, C., Millward, G., Arge, C., et al. (2015). Ensemble modeling of the 23 july 2012 coronal mass ejection. *Space Weather*, *13*(10), 611–625. https://doi.org/10.1002/2015SW001232

Curto, J., Cardús, J., Alberca, L., & Blanch, E. (2007). Milestones of the iaga international service of rapid magnetic variations and its contribution to geomagnetic field knowledge. *Earth Planets and Space*, *59*(5), 463–471. https://doi.org/10.1186/BF03352708

Durgonics, T., Komjathy, A., Verkhoglyadova, O., Shume, E. B., Benzon, H.-H., Mannucci, A. J., et al. (2017). Multiinstrument observations of a geomagnetic storm and its effects on the arctic ionosphere: A case study of the 19 february 2014 storm. *Radio Science*, *52*(1), 146–165. https://doi.org/10.1002/2016RS006106

Engebretson, M. J., Yang, L., Steinmetz, E. S., Pilipenko, V. A., Moldwin, M. B., McCuen, B. A., et al. (2024). Extreme geomagnetic disturbances (gmds) observed in eastern arctic Canada: Occurrence characteristics and solar cycle dependence. *Journal of Geophysical Research: Space Physics*, *129*(1), e2023JA031643. https://doi.org/10.1029/2023JA031643

Friis-Christensen, E., McHenry, M., Clauer, C., & Vennerstrøm, S. (1988). Ionospheric traveling convection vortices observed near the polar cleft: A triggered response to sudden changes in the solar wind. *Geophysical Research Letters*, *15*(3), 253–256. https://doi.org/10.1029/GL015i003p00253

Glassmeier, K.-H., Hönisch, M., & Untiedt, J. (1989). Ground-based and satellite observations of traveling magnetospheric convection twin vortices. *Journal of Geophysical Research*, *94*(A3), 2520–2528. https://doi.org/10.1029/JA094iA03p02520

Grandin, M., Aikio, A. T., & Kozlovsky, A. (2019). Properties and geoeffectiveness of solar wind high-speed streams and stream interaction regions during solar cycles 23 and 24. *Journal of Geophysical Research: Space Physics*, *124*(6), 3871–3892. https://doi.org/10.1029/2018ja026396

Guarnieri, F. L., Tsurutani, B. T., Echer, E., & Gonzalez, W. D. (2007). Geomagnetic activity and auroras caused by high-speed streams: A review. *Advances in Geosciences*, *8*, 91–102. Solar Terrestrial (ST). https://doi.org/10.1142/9789812708939_0006

Hajra, R. (2022). Intense geomagnetically induced currents (gics): Association with solar and geomagnetic activities. *Solar Physics*, *297*(1), 14. https://doi.org/10.1007/s11207-021-01945-8

Hutchinson, J. A., Wright, D., & Milan, S. (2011). Geomagnetic storms over the last solar cycle: A superposed epoch analysis. *Journal of Geophysical Research*, *116*(A9). https://doi.org/10.1029/2011JA016463

Huttunen, K., Kilpua, S., Pulkkinen, A., Viljanen, A., & Tanskanen, E. (2008). Solar wind drivers of large geomagnetically induced currents during the solar cycle 23. *Space Weather*, *6*(10). https://doi.org/10.1029/2007SW000374

Iyemori, T. (1990). Storm-time magnetospheric currents inferred from mid-latitude geomagnetic field variations. *Journal of Geomagnetism and Geoelectricity*, *42*(11), 1249–1265. https://doi.org/10.5636/jgg.42.1249

Joselyn, J., & Tsurutani, B. (1990). Geomagnetic sudden impulses and storm sudden commencements: A note on terminology. *Eos, Transactions American Geophysical Union*, *71*(47), 1808–1809. https://doi.org/10.1029/90EO00350

Juusola, L., Vanhamäki, H., Viljanen, A., & Smirnov, M. (2020). Induced currents due to 3d ground conductivity play a major role in the interpretation of geomagnetic variations. *Annales Geophysicae*, *38*(5), 983–998. https://doi.org/10.5194/angeo-38-983-2020

Juusola, L., Viljanen, A., Dimmock, A. P., Kellinsalmi, M., Schillings, A., & Weygand, J. M. (2023). Drivers of rapid geomagnetic variations at high latitudes. *Annales Geophysicae*, *41*(1), 13–37. https://doi.org/10.5194/angeo-41-13-2023

Juusola, L., Viljanen, A., Van De Kamp, M., Tanskanen, E., Vanhamäki, H., Partamies, N., & Kauristie, K. (2015). High-latitude ionospheric equivalent currents during strong space storms: Regional perspective. *Space Weather*, *13*(1), 49–60. https://doi.org/10.1002/2014SW001139

Kamide, Y., Baumjohann, W., Daglis, I., Gonzalez, W., Grande, M., Joselyn, J., et al. (1998). Current understanding of magnetic storms: Storm-substorm relationships. *Journal of Geophysical Research*, *103*(A8), 17705–17728. https://doi.org/10.1029/98JA01426

Kataoka, R., & Pulkkinen, A. (2008). Geomagnetically induced currents during intense storms driven by coronal mass ejections and corotating interacting regions. *Journal of Geophysical Research*, *113*(A3). https://doi.org/10.1029/2007JA012487

Kellinsalmi, M., Viljanen, A., Juusola, L., & Käki, S. (2022). The time derivative of the geomagnetic field has a short memory. *Annales Geophysicae*, *40*(4), 545–562. https://doi.org/10.5194/angeo-40-545-2022

Kilpua, E., Koskinen, H. E., & Pulkkinen, T. I. (2017). Coronal mass ejections and their sheath regions in interplanetary space. *Living Reviews in Solar Physics*, *14*, 1–83. https://doi.org/10.1007/s41116-017-0009-6

Kim, H., Lessard, M. R., Jones, S. L., Lynch, K. A., Fernandes, P. A., Aruliah, A. L., et al. (2017). Simultaneous observations of traveling convection vortices: Ionosphere-thermosphere coupling. *Journal of Geophysical Research: Space Physics*, *122*(5), 4943–4959. https://doi.org/10.1002/2017JA023904

Kim, H.-J., Lee, D.-Y., & Lyons, L. (2008). Are repetitive particle injections during high-speed solar wind streams classic substorms? *Journal of Geophysical Research*, *113*(A8). https://doi.org/10.1029/2007JA012847

King, J., & Papitashvili, N. (2005). Solar wind spatial scales in and comparisons of hourly wind and ace plasma and magnetic field data. *Journal of Geophysical Research*, *110*(A2). https://doi.org/10.1029/2004ja010649

Kumar, S., & Kumar, S. (2020). Equatorial ionospheric tec and scintillations under the space weather events of 4–9 september 2017: M-Class solar flares and a g4 geomagnetic storm. *Journal of Atmospheric and Solar-Terrestrial Physics*, *209*, 105421. https://doi.org/10.1016/j.jastp.2020.105421

Loewe, C., & Prölss, G. (1997). Classification and mean behavior of magnetic storms. *Journal of Geophysical Research*, *102*(A7), 14209–14213. https://doi.org/10.1029/96JA04020

Marshall, R., Pearce, E., Waters, C., & Terkildsen, M. (2022). Forecasting gic activity associated with solar wind shocks for the australian region power network. *Space Weather*, *20*(11), e2021SW003029. https://doi.org/10.1002/2015SW001263

Milan, S., Imber, S., Fleetham, A., & Gjerloev, J. (2023). Solar cycle and solar wind dependence of the occurrence of large db/dt events at high latitudes. *Journal of Geophysical Research: Space Physics*, *128*(4), e2022JA030953. https://doi.org/10.1029/2022JA030953

Milan, S., Mooney, M., Bower, G., Fleetham, A., Vines, S., & Gjerloev, J. (2023). Solar wind-magnetosphere coupling during high-intensity long-duration continuous ae activity (hildcaa). *Journal of Geophysical Research: Space Physics*, *128*(11), e2023JA032027. https://doi.org/10.1029/2023JA032027

Pawlowicz, R. (2020). M_map: A mapping package for matlab, version 1.4m. www.eoas.ubc.ca/~rich/map.html. [Computer software] (last accessed 22 january 2024)

Pedersen, M., Juusola, L., Vanhamäki, H., Aikio, A., & Viljanen, A. (2024). Software for detection of geomagnetic storms and storm phases in MATLAB (Version v1). *Zenodo*. [Software]. https://doi.org/10.5281/zenodo.12699343

Pedersen, M., Vanhamäki, H., & Aikio, A. (2023). Comparison of field-aligned current responses to HSS/SIR, sheath, and magnetic cloud driven geomagnetic storms. *Geophysical Research Letters*, *50*(11), e2023GL103151. https://doi.org/10.1029/2023GL103151

Pedersen, M., Vanhamäki, H., Aikio, A., Waters, C., Gjerloev, J., Käki, S., & Workayehu, A. (2022). Effect of ICME-driven storms on field-aligned and ionospheric currents from AMPERE and SuperMAG. *Journal of Geophysical Research: Space Physics*, *127*(8), e2022JA030423. https://doi.org/10.1029/2022JA030423

Pedersen, M., Vanhamäki, H., Aikio, A. T., Käki, S., Workayehu, A. B., Waters, C. L., & Gjerloev, J. W. (2021). Field-aligned and ionospheric currents by AMPERE and SuperMAG during HSS/SIR-driven storms. *Journal of Geophysical Research: Space Physics*, *126*(11), e2021JA029437. https://doi.org/10.1029/2021JA029437

Pulkkinen, A., Amm, O., & Viljanen, A. (2003). Ionospheric equivalent current distributions determined with the method of spherical elementary current systems. *Journal of Geophysical Research*, *108*(A2). https://doi.org/10.1029/2001JA005085

Pulkkinen, A., Bernabeu, E., Thomson, A., Viljanen, A., Pirjola, R., Boteler, D., et al. (2017). Geomagnetically induced currents: Science, engineering, and applications readiness. *Space Weather*, *15*(7), 828–856. https://doi.org/10.1002/2016SW001501

Richardson, I. G., & Cane, H. (2024). Near-Earth interplanetary coronal mass ejections since january 1996. *Harvard Dataverse*. [Dataset]. https://doi.org/10.7910/DVN/C2MHTH

Richardson, I. G., & Cane, H. V. (2010). Near-earth interplanetary coronal mass ejections during solar cycle 23 (1996–2009): Catalog and summary of properties. *Solar Physics*, *264*(1), 189–237. https://doi.org/10.1007/s11207-010-9568-6

Robbrecht, E., & Berghmans, D. (2004). Automated recognition of coronal mass ejections (cmes) in near-real-time data. *Astronomy and Astrophysics*, *425*(3), 1097–1106. https://doi.org/10.1051/0004-6361:20041302

Sandhu, J., Rae, I., & Walach, M.-T. (2021). Challenging the use of ring current indices during geomagnetic storms. *Journal of Geophysical Research: Space Physics*, *126*(2), e2020JA028423. https://doi.org/10.1002/jgra.50576

Schillings, A., Palin, L., Opgenoorth, H. J., Hamrin, M., Rosenqvist, L., Gjerloev, J., et al. (2022). Distribution and occurrence frequency of db/dt spikes during magnetic storms 1980–2020. *Space Weather*, *20*(5), e2021SW002953. https://doi.org/10.1029/2021SW002953

Smith, A. W., Forsyth, C., Rae, J., Rodger, C. J., & Freeman, M. P. (2021). The impact of sudden commencements on ground magnetic field variability: Immediate and delayed consequences. *Space Weather*, *19*(7), e2021SW002764. https://doi.org/10.1029/2021SW002764

Sugiura, M. (1963). Hourly values of equatorial dst for the igy. *Technical Report D*.

Tanskanen, E., Viljanen, A., Pulkkinen, T., Pirjola, R., Häkkinen, L., Pulkkinen, A., & Amm, O. (2001). At substorm onset, 40% of al comes from underground. *Journal of Geophysical Research*, *106*(A7), 13119–13134. https://doi.org/10.1029/2000JA900135

Tsurutani, B. T., Gonzalez, W. D., Gonzalez, A. L., Guarnieri, F. L., Gopalswamy, N., Grande, M., et al. (2006). Corotating solar wind streams and recurrent geomagnetic activity: A review. *Journal of Geophysical Research*, *111*(A7). https://doi.org/10.1029/2005JA011273

Tsurutani, B. T., Gonzalez, W. D., Guarnieri, F., Kamide, Y., Zhou, X., & Arballo, J. K. (2004). Are high-intensity long-duration continuous ae activity (hildcaa) events substorm expansion events? *Journal of Atmospheric and Solar-Terrestrial Physics*, *66*(2), 167–176. https://doi.org/10.1016/j.jastp.2003.08.015

Vanhamäki, H., & Juusola, L. (2020). Introduction to spherical elementary current systems. In *Ionospheric multi-spacecraft analysis tools: Approaches for deriving ionospheric parameters* (pp. 5–33).

Vennerstrom, S., Lefevre, L., Dumbović, M., Crosby, N., Malandraki, O., Patsou, I., et al. (2016). Extreme geomagnetic storms–1868–2010. *Solar Physics*, *291*(5), 1447–1481. https://doi.org/10.1007/s11207-016-0897-y

Viljanen, A., Nevanlinna, H., Pajunpää, K., & Pulkkinen, A. (2001). Time derivative of the horizontal geomagnetic field as an activity indicator. *Annales Geophysicae*, *19*(9), 1107–1118. https://doi.org/10.5194/angeo-19-1107-2001

Walach, M.-T., & Grocott, A. (2019). Superdarn observations during geomagnetic storms, geomagnetically active times, and enhanced solar wind driving. *Journal of Geophysical Research: Space Physics*, *124*(7), 5828–5847. https://doi.org/10.1029/2019JA026816

Wanliss, J. A., & Showalter, K. M. (2006). High-resolution global storm index: Dst versus sym-h. *Journal of Geophysical Research*, *111*(A2). https://doi.org/10.1029/2005JA011034

Weaver, M. (2004). Halloween space weather storms of 2003.

Webb, D. F., & Howard, T. A. (2012). Coronal mass ejections: Observations. *Living Reviews in Solar Physics*, *9*(1), 1–83. https://doi.org/10.12942/lrsp-2012-3

Yermolaev, Y. I., Lodkina, I., Nikolaeva, N., & Yermolaev, M. Y. (2014). Influence of the interplanetary driver type on the durations of the main and recovery phases of magnetic storms. *Journal of Geophysical Research: Space Physics*, *119*(10), 8126–8136. https://doi.org/10.1002/2014JA019826

Yokoyama, N., & Kamide, Y. (1997). Statistical nature of geomagnetic storms. *Journal of Geophysical Research*, *102*(A7), 14215–14222. https://doi.org/10.1029/97JA00903

Zhang, J., Wang, C., Sun, T., Liu, C., & Wang, K. (2015). Gic due to storm sudden commencement in low-latitude high-voltage power network in China: Observation and simulation. *Space Weather*, *13*(10), 643–655. https://doi.org/10.1002/2015SW001263

Zhou, Y.-L., & Lühr, H. (2022). Initial response of nightside auroral currents to a sudden commencement: Observations of electrojet and substorm onset. *Journal of Geophysical Research: Space Physics*, *127*(4), e2021JA030050. https://doi.org/10.1029/2021JA030050